Tectonophysics 579 (2012) 88–103

Contents lists available at SciVerse ScienceDirect

Tectonophysics

journal homepage: www.elsevier.com/locate/tecto

Bimodal behavior of extended continental lithosphere: Modeling insight and application to thermal history of migmatitic core complexes

F.L. Schenker *, T. Gerya, J.-P. Burg

Department of Earth Sciences, ETH Zurich, Sonnegstrasse 5, CH-8092, Zurich, Switzerland

ARTICLE INFO

Article history:
Received 6 March 2012
Received in revised form 27 June 2012
Accepted 4 July 2012
Available online 26 July 2012

Keywords:
Extensional migmatitic core complex
Naxos migmatitic dome
Rhodope metamorphic core complexes
Collisional vs. asthenospheric heat source
Pressure–temperature–time path
Flat Moho

ABSTRACT

Extensional migmatitic core complexes (MiCC) expose partially molten crustal rocks exhumed during post-thickening extension. Low heat flow in active collisional mountains suggests that there is (i) either input from extra-crustal heat sources or (ii) under-assessment of the pre-extensional collisional-heat content to form high grade metamorphic core complexes. We evaluate these two hypotheses by varying thermal gradients and crustal thicknesses of two-dimensional, thermo-mechanical, numerical models simulating the extension of a stratified lithosphere. For Moho-temperatures <700 °C and crustal thicknesses >35 and ≤50 km, extension leads to a rifting mode dictated by the upwelling of the asthenosphere. In that case, no MiCC is formed. For Moho-temperatures >700 °C and/or crustal thicknesses >60 km, extension develops MiCC while maintaining a flat Moho, similar to wide extensional systems such as the Aegean and the Basin and Range. However, when crustal strain softening is switched on, it produces for both mentioned conditions MiCCs with similar crustal geometries, testifying that partial melting in MiCCs can result from both extra-crustal, syn-extensive heat (asthenospheric advection) and collisional heat. Typically, MiCCs induced by asthenospheric-heat show the sequence lower crustal migmatization, doming and crustal Ultra-High-Temperature (UHT) conditions and mantle melting in a short temporal range (from 5 to 10 model-Ma) after asthenospheric upwelling; the convective migmatitic dome is shifted horizontally with respect to the asthenospheric culmination and dome migmatites experience isobaric heating to peak conditions. In contrast, collisional-heat induced MiCCs exhibit pre-extensional migmatization and subsequent doming (at 3–4 model-Ma). In this case, the asthenosphere, generating lower crustal UHT conditions and mantle melts, upwells lately and is not symptomatic for MiCC formed in short extensional pulses (<12 model-Ma); convective core migmatites experience isothermal decompression during doming. The Eocene Rhodope domes exemplify asthenosphere-heat induced MiCCs. The Miocene Naxos dome is instead interpreted as a collisional-heat induced MiCC.

1. Introduction

Thermal and structural domes cored by partially molten crustal rocks (the migmatites) are in many cases extensional migmatitic core complexes (MiCC). The major detachment bounding such domes accommodates most of the crustal extension and unroofing of the migmatites (e.g. Davis and Coney, 1979). Buoyant migmatites have a dynamic role in exhuming mid-crustal rocks, supporting vertical movements and the up arched architecture (Burg and Vanderhaeghe, 1993; Gautier et al., 1990; Ledru et al., 2001). Although extensional MiCCs act as important mass and heat redistribution vectors in many extended crusts (e.g. Alpine-Himalayan Belt (e.g. Lister et al., 1984), Hercynian (Burg et al., 1994; Echtler and Malavieille, 1990; Van Den Driessche and Brun, 1992), Caledonian (Andersen et al., 1991; Norton, 1986; Seranne and Seguret, 1987)), no general consensus is found in identifying the heat source responsible for migmatization and for the metamorphic overprint of the dome carapace (Whitney et al., 2004b). Two main heat sources are distinguished: a) inherited collisional heat due to tectonic imbrication of heat producing radiogenic crustal material (e.g. Bousquet et al., 1997; Engi et al., 2001; Goffe et al., 2003; Huerta et al., 1998; Jamieson et al., 1998; Vanderhaeghe et al., 2003) and/or from viscous heating (Burg and Gerya, 2005; Kincaid and Silver, 1996; Whittington et al., 2009) and b) syn-extensional diffusive heat. The latter is typical for thermal relaxation (England and Thompson, 1984) or for heat sourcing in an upwelled asthenosphere. An advective origin such as voluminous magmatic events (e.g. Von Blanckenburg and Davies, 1995) with/without spasmodic fluid pulses (e.g. Camacho et al., 2005) is possible, but is not treated in this study. Each of these processes exhibits different time-scales of heat transport (England and Thompson, 1984). The metamorphic culmination reached with partial melting is achieved at different stages according to source and heat transport mechanisms. Because the mechanical response of the lithosphere to partial melting can be drastic, due to severe rheological

* Corresponding author. Tel.: +41 446327100; fax: +41 44 632 10 30.
E-mail addresses: filippo.schenker@erdw.ethz.ch (F.L. Schenker), taras.gerya@erdw.ethz.ch (T. Gerya), jean-pierre.burg@erdw.ethz.ch (J.-P. Burg).

0040-1951/$ – see front matter © 2012 Elsevier B.V. All rights reserved.
http://dx.doi.org/10.1016/j.tecto.2012.07.002

changes of the rocks (reduction in strength by 2–3 orders of magnitude at the threshold between the solid and partially molten rocks and 5–7 orders of magnitude at the threshold of partially molten rocks and magmas (e.g. Clauser and Huenges, 1995; Rosenberg, 2001; Vanderhaeghe, 2009; Vandermolen and Paterson, 1979; Vigneresse et al., 1996)), the timing of migmatization is fundamental to understand the evolution of extensional settings. The rheological behavior depends on interdependent intrinsic properties such as composition and density and on extrinsic conditions such as pressure and temperature. Temperature-driven crustal melting weakens the strength of the lithosphere and simultaneously decreases the density of the rock, facilitating vertical and horizontal isostatic compensations and, therefore, affecting the mechanics of the lithosphere and the style of extensional patterns. The aim of this study is to characterize timing, rheological effects and heat sources of migmatization in extending continental lithospheres with different initial thicknesses and thermal contents, focusing on MiCC formation.

We treat the problem numerically, with a thermo-mechanical code able to link the extrinsic conditions (*P* and *T*) and intrinsic properties (E, ρ and η) (abbreviations in Table 1). We use a visco-elasto-plastic rheology in a starting five layer setup (atmosphere, upper crust, lower crust, lithospheric mantle and asthenospheric mantle). The setup is designed to simulate the complete section of the continental lithosphere; this is necessary to consider the respective roles of the lithospheric and asthenospheric mantles. Partial melting is not preset, but it is simulated with phase transformations when the *P* and *T* of rocks enter in the supra-solidus regime. This is the key point in our study since it allows evaluating whether inherited high thermal conditions are really required to form MiCCs or if those can be generated from a cold lithosphere, with the heat necessary for migmatization emanating from diffusive mantle heating. The timing of melting in the crust and/or in the mantle becomes an important criterion to compare our simulations to geological cases. The thermal evolution of the MiCCs is extracted from calculation of metamorphic *P*–*T*–time paths of crustal rocks.

We explore the thermal and mechanical evolution of an extending continental lithosphere by changing the initial thermal conditions and the initial thicknesses of the crust. Concretely, the main questions we want to answer are: How is the mechanical response to different thermal conditions at the onset of extension? At what stage of extension does migmatization start and what is the mechanical response to it? Finally, is the heat responsible for crustal migmatization inherited from earlier collision (in our study collisional heat is imposed with the initial thermal gradient) or sourced from a syn-extension diffusive thermal relaxation?

The systematic variation of geotherms reveals a bimodal behavior of the lithosphere: (1) a rifting mode for initial Moho-temperatures (T_{MOHO}) < 700 °C and initial crustal thicknesses (h_0) between and including 35 and 50 km and (2) a lower-crustal-doming mode for T_{MOHO} > 700 °C and/or h_0 > 60 km. MiCCs were obtained in both cases, provided strain softening is implemented. However, mode (1) MiCCs have different Moho topography and thermo-mechanical histories than mode (2) MiCCs. This shows that MiCCs can also develop in a cold lithosphere, the heat necessary for migmatization being sourced from the asthenospheric mantle. The two end-members find geological affinities with the Rhodope migmatite dome complex and with the Naxos dome, respectively.

Table 1
Abbreviation and units.

Symbol	Meaning
A_D (MPa^{-n} s^{-1})	Material constant
Cp (J kg^{-1} K^{-1})	Isobaric heat capacity
$c_{1,2}$	Cohesion coefficient
E (kJ mol^{-1})	Activation energy
$F_{1,2}$	Angle of internal friction
G (Pa)	Plastic potential
H_r, H_a, H_s (W m^{-3})	Radioactive, adiabatic and shear heat production
h_{crust}	Initial thickness of the crust
k (W m^{-1} K^{-1})	Thermal conductivity
M	Volume fraction of melt
n	Stress exponent
P, P_{solid} (Pa)	Dynamic pressure (mean stress on solids)
P_{fluid} (Pa)	Pore fluid pressure
Q_L (Kj/kg^{-1})	Latent heat of melting
t (s)	Time
T (K)	Temperature
$T_{liquidus}, T_{solidus}$ (K)	Liquidus and solidus temperature of a rock
V (J MPa^{-1} mol^{-1})	Activation volume
vx, vz (m s^{-1})	Horizontal and vertical components of velocity vector
x, z (m)	Horizontal and vertical coordinates
Z	Viscoelasticity factor
α (K^{-1})	Thermal expansion coefficient
β (Pa^{-1})	Compressibility coefficient
χ (s^{-1})	Plastic multiplier
ε_{ij} (s^{-1})	Components of the strain rate tensor
η (Pa s)	Viscosity
λ	Pore fluid pressure coefficient: λ = Pfluid/Psolid
μ (Pa)	Shear modulus
ρ (kg m^{-3})	Density
σ_{II} (Pa^2)	Second invariant of the deviatoric stress tensor
σ_{ij} (Pa)	Components of the deviatoric stress tensor

2. Numerical modeling of migmatitic core complexes

2.1. Previous models

1D numerical investigations with thin sheet approximations analyzed the first-order lithosphere-scale behavior during extensive divergence (Buck, 1991), predicting metamorphic core complexes with high heat flow. The early mechanical, 2D numerical studies on extensional domes have been employing simplified visco-plastic models (Buiter et al., 2008; Huismans et al., 2005), concentrating mainly on symmetric/asymmetric doming, fault tectonics and deformation of domes and the surrounding rocks. Subsequent work (Tirel et al., 2004, 2008, 2009) showed that high initial thermal gradients (T_{Moho} > 800 °C) induce doming by enhancing lower crustal flow that fills up the dome core. Work taking into account lower crustal melting established that the temperature-dependent melt fraction (affecting both density and viscosity) has little effect on the formation of crustal-scale MiCCs (Rey et al., 2009), but influences the core dynamic and architecture (Rey et al., 2011). The geotherm of these simulations with melt was fixed to optimize the melt fraction at values (peak melt fraction of 35% at the Moho) similar to natural cases. Huet et al. (2011) investigated the effect of both structural and thermal orogenic heritage on extensional tectonics, finding that metamorphic core complexes can also develop in a cold lithosphere with inverted density stratification (strong mafic layer above a weak lower crust).

While other works on metamorphic extensional domes focused separately either on the effect of migmatites in a setup where melt is prescribed or on the influence of thermal heritage without partial melting, our study combined the thermal heritage with partial melting possibly absent at initial conditions. Melting was generated at the appropriate P and T conditions defined by the solidus of each mineral phase (Table 2). The fully coupled thermo-mechanical code is designed for phase transformations and includes the drops in viscosity and density of partially molten rocks for both the crustal lithologies simulating the migmatites and for mantle lithologies. Consequently, mantle melting can be generated, yielding a fundamental time-constraint for magmatism in extensional settings; this point has importance since syn-extensional magmatism with a mantle signature is reported in most of widely extended regions (Aegean (e.g. Altherr et al., 1988), Rhodope (e.g. Jones et al., 1992), Basin and Range (e.g. Hawkesworth et al., 1995)).

Table 2
Material properties used in the 2D modeling (C_p = 1000 J/kg, $\alpha = 3\times10^{-5}$ K^{-1}, $\beta = 1\times10^{-5}$ Mpa^{-1} initial values for all rock types). Abbreviations as in Table 1. References [b]: (1) Turcotte and Schubert (2002), (2) Clauser and Huenges (1995), (3) Schmidt and Poli (1998), (4) Ranalli (1995), (5) Hess (1989). Viscosity of the molten rocks with M > 0.1 is set to a lower cutoff viscosity value of 10^{17} Pa s. Air/water/molten rocks have constant viscosity, therefore no E, n, A_D, V are needed.

Material	Color	ρ_0 (kg m^{-3})	k (W m^{-1} K^{-1})	$T_{solidus}$ (K)	$T_{liquidus}$ (K)	Q_L (kJ/kg)	H_r (μWm^{-3})	Flow law	E (kJ mol^{-1})	N	A_D (MPa^{-n} s^{-1})	V (J/(MPa mol))	μ (GPa)
Air (atmosphere)	White	1	20	–	–	0	0	10^{18} Pa s	–	–	–	–	10
Water	Blue	1000	20	–	–	0	0	10^{17} Pa s	–	–	–	–	10
Upper crust (sediments)	Orange	2600 (solid)	[0.64 + 807/(T + 77)] × exp(0.00004P_{MPa})	889 + 17,900/(P + 54) + 20,200/(P + 54)^2 at P < 1200	1262 + 0.09P	0	1.75	Wet quartzite	154	2.3	$10^{-3.5}$	0	10
Migmatitic upper crust	Black	2500 (molten)	[0.64 + 807/(T + 77)] × exp(0.00004P_{MPa})	MPa, 831 + 0.06P at P > 1200 MPa		300	1.75	10^{17} Pa s	–	–	–	–	10
Lower crust	Gray	2700 (solid)	[0.64 + 807/(T + 77)] × exp(0.00004P_{MPa})	889 + 17,900/(P + 54) + 20,200/(P + 54)^2 at P < 1200	1262 + 0.09P	0	1.75	Wet quartzite	154	2.3	$10^{-3.5}$	0	25
Migmatitic lower crust	Purple	2500 (molten)	[0.64 + 807/(T + 77)] × exp(0.00004P_{MPa})	MPa, 831 + 0.06P at P > 1200 MPa		300	1.75	10^{17} Pa s	–	–	–	–	25
Lithosphere-asthenosphere mantle	Blue-violet	3300 (solid)	[0.73 + 1293/(TK + 77] × exp(0.00004P_{MPa})	1394 + 0.132899P − 0.000005014P^2 at P < 10,000 Mpa,	2073 + 0.114P	0	0.022	Dry olivine	532	3.5	10^{44}	8	67
Molten mantle	Red	2900 (molten)	[0.73 + 1293/(TK + 77] × exp(0.00004P_{MPa})	2212 + 0.030819(P–10,000) at P > 10,000 MPa		400	0.022	10^{17}Pa s	–	–	–	–	67
References[b]		1	2	3,5	3,5	1,5	1	4	4	4	4	4	1

2.2. Numerical code and model setup

We employed the 2D I2ELVIS code based on finite differences with a marker-in-cell technique (Gerya and Yuen, 2007). The accurate conservative solutions of the governing equations are computed on a rectangular fully staggered Eulerian grid. The code is designed for a thermomechanical visco-elasto-plastic rheological model identical to that described in Gerya and Burg (2007); detailed equations are given in Appendix A. The software includes frictional/viscous and radiogenic heating and determines the evolving non-steady state temperature distribution and heat flow, along with the pressure-temperature-time trajectories of material points. The numerical model simulates partial melting by (i) decreasing the density with increasing melt fraction, (ii) decreasing the effective viscosity for volumetric melt fractions > 0.1, and (iii) taking into account thermal effects of the latent heat. Other processes associated with partial melting, such as solid/melt segregation, are neglected because they occur on spatial and temporal scales that have no influence on the results described in this study. The volumetric melt fraction increases linearly with T at P–T conditions between wet solidus and dry liquidus of the considered rock type. Equations of liquidus and solidus are given in Table 2. No rheological weak zone was prescribed. Strain localization along shear zones is triggered by shear heating and/or strain softening (when imposed) that both decrease the strength due to local pressure drop (detail in Appendix A.1). Strain softening is achieved with a linear decrease of the coefficient of internal friction of the Coulomb failure criterion during increasing strain (Appendix A.2).

The initial model size is scaled to encompass 300 km × 160 km with a 0.5 km × 0.5 km cell grid covering five rheological layers: the atmosphere, the wet-quartzitic upper crust, the wet-quartzitic lower crust, the dry olivine lithospheric mantle and asthenospheric mantle (Fig. 1). Similar rheological conditions were previously used to model crustal thickening in continental plate collisions (Burov and Yamato, 2008). Temperature-dependent phase transformations generate new phases that are not pre-set: partially molten upper and lower crusts and partially molten mantle. For better visualization of deformation the lithosphere — asthenosphere transition is arbitrarily prescribed on Lagrangian markers between 1000 and 1300 °C. However, the same flow law, density and melting relationships are employed for both lithospheric and asthenospheric mantles. Crustal thickness before extension was systematically varied from 70 to 35 km, keeping a ratio of 3/2 between upper and lower crust for consistency. A total extension velocity of 1.6 cm/a was applied at the two lateral boundaries, taking the extension rate from GPS measurements on the active Corinth rift (Briole et al., 2000). Different linear geotherms were imposed for the initial thermal crustal conditions, with the initial thermal state of the lithosphere being not in equilibrium. However, the temperature at the base of the model, within the asthenosphere, is kept constant at 1400 °C. Table 2 lists the material properties used in the numerical experiments.

Free-slip conditions are imposed on the right and left boundaries. The top surface is computed dynamically as a free surface by using the top layer with viscosity and density of air and/or water (Table 2). The large viscosity contrast minimizes shear stresses at the top of the crust with the practical effect of simulating a free surface (e.g. Schmeling et al., 2008). The upper interface of the crust is treated as a free erosion/sedimentation surface that evolves dynamically according to the transport equation solved on the Eulerian coordinates (details in Appendix A.3). The gross-scale sedimentation rate and the erosion rate are kept constant during experiments. The bottom boundary has an infinity-like external free slip condition (Burg and Gerya, 2005) and permits vertical material and heat flow.

3. Results

The thermal gradients were varied between 10 °C/km and 22.8 °C/km, covering a range of values typical for cold to intermediate

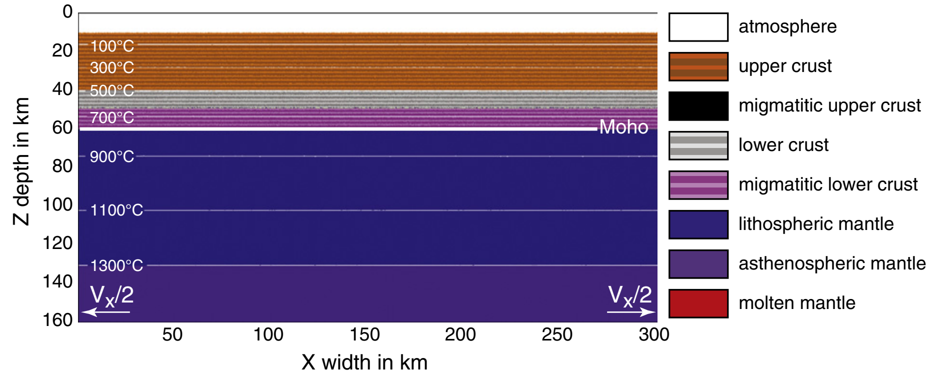

Fig. 1. Model setup. Migmatitic upper and lower crust and molten mantle are not prescribed. They form with temperature dependent phase transformations. Lithological/material properties in Table 2. V_x = total extension velocity.

temperature in the Andes (e.g. Lachenbruch and Sass, 1978). Our values are also in the range of estimated Himalayan geotherms, such as the 22.5 °C/km extrapolated from radiometric dating and metamorphic mineral assemblages in a “hot” orogenic terrain (Burg et al., 1998) and the 25 °C/km from extrapolated models (Artemieva and Mooney, 2001).

The systematic variation of the thermal conditions and initial thickness of the crust yielded two extensional modes (Fig. 2): (i) “Rifting” for $T_{MOHO}<700$ °C and $35<h_0\leq 50$ km, and (ii) “Lower-crustal-doming” for $T_{MOHO}>700$ °C or $h_0>60$ km. At intermediate conditions, asthenospheric upwelling, typical of the rifting mode, was coeval and laterally offset with respect to lower crustal doming. This intermediate mode is called “disharmonic doming”.

3.1. Rifting mode

Rifting is the dominant mode for $T_{MOHO}<700$ °C for an initially normal to moderately thickened crust ($35\ \text{km}<h_0\leq 50$ km). Extension is first accommodated by conjugate shear zones in the upper crust and in the upper mantle and by diffuse flow in the lower crust and in the asthenospheric mantle. After 4.2 model-Ma (m-Ma) several shear zones in the upper mantle became dominant, defining a conjugate, upward converging set of normal shear zones into the lithospheric mantle (Fig. 3a). These shear zones, which meet 7 km below the Moho depth, broadly bound a triangle in which the lithospheric mantle thinned, making space for upwelling of the asthenosphere and, as a consequence, up-arching of the mantle isotherms. At the same time, and above the convergence point, the same shear zones controlled a Moho-depression (up to 5 km stepping) filled by the lower crust (Fig. 3a, t = 6.5 m-Ma). The propagation of these shear zones through the crust delimited an inverted, hanging wall trapezoidal region with no or indiscernible internal strain. This part of the crust preserved its initial thickness while the adjacent crust was thinned. Isotherms were bent downward in this crustal region. At 8.6 m-Ma (arrows in Fig. 3a), each flank of the Moho depression shifted sideway, away from their original position, while the lower crust of the formerly unstrained trapezoidal region was thinned into a necking zone. Two surface depressions (sedimentary basins) formed above each flank of the Moho depression and migrated apart with the shifting Moho-depression flanks. The thermal gradient was sufficiently increased in the lower crust to produce partial melting (pink lithology in Fig. 3a, t = 6.5, 8.6 and 10.2 m-Ma). The 900 °C isotherm, bounding UHT conditions (leading to granulite facies rocks), reached the bottom of the crust at 8.6 m-Ma. Further extension produced melting in the decompressed asthenosphere (Fig. 3a, t = 10.2 m-Ma). Asthenospheric upwelling bended the Moho upward (Fig. 3a, t = 10.2 m-Ma), shifting deformation in the central region of the model and creating there a new basin. Note that even if the asthenosphere reached the base of the crust, no oceanization occurred after 163.2 km of extension (Fig. 3a, t = 10.2 m-Ma); the continental crust was still 12–15 km thick, with a relatively thick upper crust. Neither the migmatites nor rocks experiencing UHT conditions were exhumed to the surface.

Integration of the mean second stress invariant with model-depth shows that the upper mantle dominates the strength of the lithosphere at cold initial conditions (Fig. 3a, t = 4.2 Ma). With ongoing extension, increasing thermal conditions gradually reduced the plastic mantle strength bringing the mean second stress invariant of the mantle at the same order of magnitude as that of the upper crust. After asthenospheric upwelling (Fig. 3a, t = 8.6 Ma), the total strength of the lithosphere resided equally in the upper crust and in the mantle.

3.2. Lower crustal doming

The imposed high initial geotherms and/or thick crust ($T_{MOHO}>$ 700 °C, $h_0>60$ km) produced a layer of partially molten crustal rocks that developed convection cells at the base of the crust. In order to ascertain the buoyant instabilities responsible for convection in the molten lower crustal layer, a range of Rayleigh numbers (RA) has been computed for different values of effective thermal expansion α, which varied in the convective layer due to temperature and melt dependence of the term (Eq. (A.27) in Appendix A.3). RA has been calculated at the onset of the convective instabilities, at 0.26 m-Ma.

$$RA=\frac{\rho_0 g\alpha(T_1-T_0)b^3}{\eta\kappa} \tag{1}$$

Where $g = 9.81$ m/s^2 is gravity, $T_1 = 1063$°K and $T_0 = 973$°K are the temperatures at the bottom and at the roof of the convective layer, respectively, $b = 8000$ m is the thickness of the convective layer and $\kappa = 1.9354\times10^{-6}$ m^2/s is the mean thermal diffusivity within the layer, $\eta = 10^{17}$ Pa s is the viscosity of the molten lower crustal rocks and $\rho_0 = 2700$ kg/m^3 is the density of the solid lower crust. Values of calculated α were varying between 5×10^{-5} in the solid crust and 5.29×10^{-4} in parts of migmatitic layer.

The critical Rayleigh number RAc was computed as follows:

$$RAc=\frac{\left(\pi^2+\frac{4\pi^2b^2}{\lambda^2}\right)^3}{\frac{4\pi^2b^2}{\lambda^2}} \tag{2}$$

with the wavelength of the convection cells λ = 11,500 m. Convection is not favored for RAC > RA because the layer is isostatically stable. The instabilities grow into convection cells for RAc < Ra. The RA

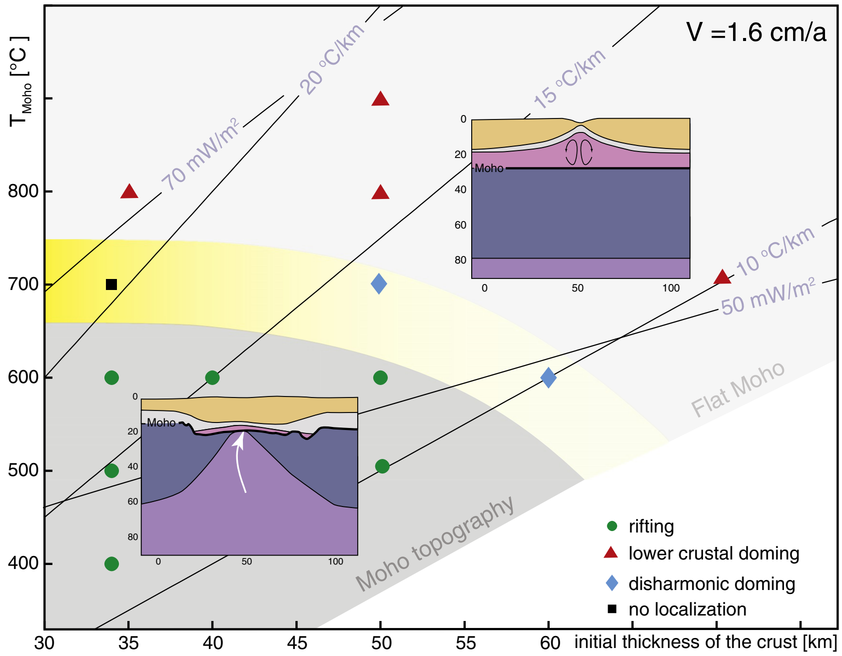

Fig. 2. Phase diagram representing the domains of rifting and lower crustal doming extensional modes as a function of initial Moho temperature and crustal thickness. Geotherms with surface heat flow of 50 mWm^{-2} and 70 mWm^{-2} from Afonso and Ranalli (2004).

for molten rocks lay mostly in the unstable range (RA > RAc), confirming the onset of convection (Fig. 4). The RA for the solid lower crust fall in the stable domain, i.e. no convection can be expected in the lower crust without melt. Partial melting induced convection by increasing the effective thermal expansion from $\alpha = 3\times10^{-5}$ 1/K (solid lower crust) to $\alpha > 5\times10^{-5}$ 1/K and by decreasing the viscosity from $\eta > 10^{19}$ Pa s (solid lower crust) to $\eta = 10^{17}$ Pa s.

At 3.9 m-Ma (Fig. 3b) the upper crust deformed and thinned between two downward converging, conjugate shear zones. Below the thinned upper crust, the convective lower crust arched upwards, delineating a lower crustal dome. The Moho topography remained flat. Stretching was homogeneously distributed in the mantle, preventing heat flux perturbations: the 900 °C- and the 1100 °C-isotherms raised flat until 8.3 m-Ma (Fig. 3b). In the crust, the isotherms contracted and arched upwards, in consistency with lower crustal doming. The partially molten core reached its maximal amplitude after 4.8 m-Ma (Fig. 3b, between t = 3.9 Ma and 8.3 Ma). Horizontal flow of the molten lower crust towards the growing dome maintained the volume and the architecture of the migmatitic core and caused overall crustal thinning. Further extension was accommodated by two major conjugate shear zones in the upper crust and the coeval dome in the lower crust. Recrystallized molten rocks surfaced along the two conjugate shear zones after amplification of the dome. The migmatites were exposed (dashed lines in Fig. 3b) and subsequently covered with sediments in the depression above the conjugate shear zones between 3.9 and 8.3 m-Ma over a horizontal length of 110 km. The bottom of the lower crust reached UHP conditions (the 900 °C isotherm) while the asthenosphere upwelled at 11.0 m-Ma. Decompression melting in the asthenosphere started at 12.3 m-Ma (Fig. 3b), which corresponded to 197.1 km of total extension. No ocean formed during the time of the simulation (12.3 m-Ma).

The initially elevated thermal condition at the MOHO reduced the mantle strength to magnitudes equivalent to crustal strength (Fig. 3b, t = 3.1 Ma) early during extension. The thermal and lithological disturbance accompanying lower-crustal doming reduced the strength of the upper crust. Consequently, the lithospheric strength that was equally-partitioned between upper crust and upper mantle, forming a "jelly-sandwich" strength model at 3.1 m-Ma, resided mostly in the viscous upper mantle after lower crustal doming (t = 8.3 Ma).

3.3. *Strain weakening experiments: asthenospheric-heat- and collisional-heat-induced MiCCs*

Strain weakening (detailed formulation in Appendix A.2) has been implemented in the two end-member cases in order to obtain asymmetric doming patterns similar to those presented by Huismans et al. (2005), Buiter et al. (2008), and Huismans and Beaumont (2011). The total extension velocity was kept constant at 1.6 cm/a, like in models without strain softening. For the rifting case, the coefficient of internal friction of the Coulomb failure decreases linearly from 0.5 to 0.07 for strains of 0.5 to 1.5 (strain is computed as an integral of second strain rate invariant (1/s) over time (s)). In the same strain window, the coefficient of internal friction decreased from 0.2 to 0.001 in the lower-crustal-doming case. The low values of the internal-friction coefficient are justified by the presence of fluids/melts in natural shear zones (produced via dehydration/melting reactions during doming) when $T_{Moho} > 700$ °C. The increased fluid/melt pressure decreases the frictional strength of rocks to almost zero (see discussions in Gerya and Burg (2007) and supplementary material in Faccenda et al. (2009)).

With strain softening the initial large-scale lithospheric behavior under different thermal conditions and thicknesses of the crust started as in Fig. 2: (i) rifting mode for $T_{MOHO} < 700$ °C and h_0 between and including 35 km and 50 km and (ii) lower-crustal-doming mode for $T_{MOHO} > 700$ °C and/or $h_0 > 60$ km. Differences arose in the subsequent extension history. Strain-softening favored asymmetric structures and triggered a MiCC in both end-members.

In case (i), migmatites that formed during rifting above the upwelling asthenosphere migrated laterally in the footwall of a localizing normal fault, forming a low angle detachment over a MiCC, which is offset by about 30 km with respect to the asthenospheric upwelling center (Fig. 5a). Since the migmatites originated above the asthenosphere, these are *asthenospheric-heat induced MiCCs*. Lateral flow of partially molten material was induced by a lithostatic pressure gradient between footwall and hanging wall. This pressure gradient was originated by a 4.5 km deep hanging wall basin. The shear zone progressively rotated to shallower dip angles with ongoing extension, due to lateral isostatic re-equilibration of the footwall. The convective migmatitic core reached melt fraction up to 30 %. The recrystallized

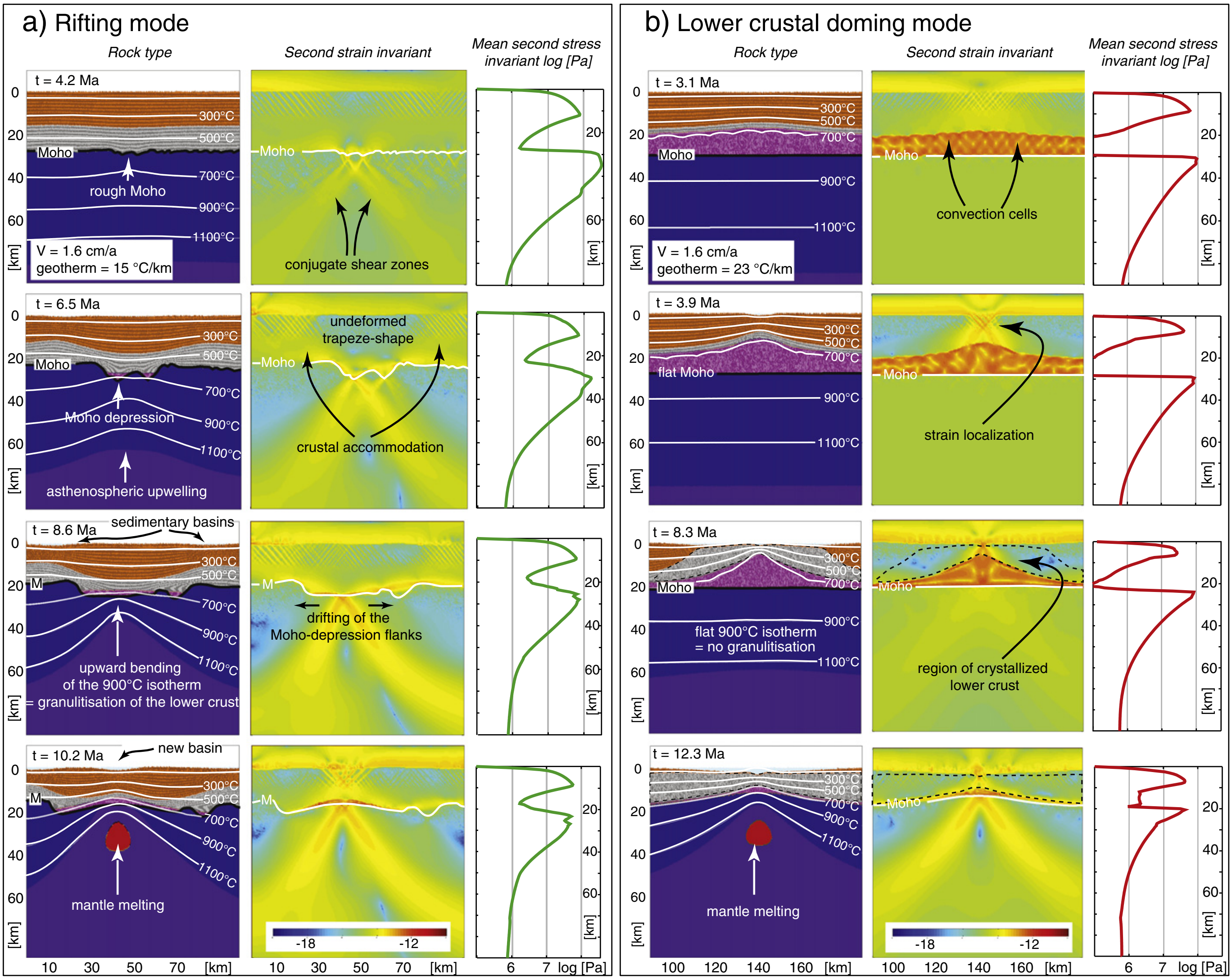

Fig. 3. Rock type, second strain invariant and mean second stress invariant at different time steps of the representative models of a) rifting ($T_{MOHO} = 500$ °C and $h_0 = 35$ km) and b) lower crustal doming mode ($T_{MOHO} = 800$ °C and $h_0 = 35$ km). The areas are enlarged to 90 × 90 km from the original 160 × 300 km of the reference model (Fig. 1). The strength profiles (right columns in a) and b) are approximated with the horizontal mean value along the length of the model of the second stress invariant with depth. The black dashed lines in b) define regions of recrystallized partially molten lower crust.

molten crust has been denudated and exposed along the detachment at 10.2 m-Ma.

A secondary crustal normal shear zone, conjugate to the principal detachment, exhumed not-migmatized lower crust without bringing it up to the surface (Fig. 5a). Differently to the detachment that roofed the migmatites, this shear zone was concave up, with a mean dip angle of 35°. This confirms that lateral flow of the partially molten crust was responsible for the isostatic rebound that rotated the major normal shear zone into a low angle detachment (Buck, 1988).

UHT (granulite facies) conditions at the base of the lower crust were reached 5 m-Ma after migmatization and migmatitic doming culminated short after, at 7.5 m-Ma. Further extension produced decompressional melting in the asthenosphere at 9.6 m-Ma (Fig. 5a) like in simulations without strain softening (Fig. 3a, t = 10.2).

In case (ii), the MiCC was exhumed along a single, low-angle detachment instead of the conjugate normal faults of simulations without strain softening (Fig. 5b). The heat responsible for partial melting is imposed by the initial thermal conditions that simulated the collisional heat before extension. These migmatitic domes are called *collisional-heat induced MiCC*. This system started asymmetrically with one single shear zone roofing the migmatitic dome. This shear zone rotated progressively through footwall isostasy and became a low-angle detachment. The exposed and tilted hanging wall defines a 1 km deep basin. The migmatites were exhumed along the detachment and reached the surface at 6.4 m-Ma. The asthenosphere upwelled after lower crustal doming at 9.4 m-Ma, with the bottom of the crust undergoing UHT metamorphic conditions at 12.5 m-Ma and mantle melting at 14.9 m-Ma. The melting region in the mantle is located underneath the migmatitic dome (Fig. 6).

3.4. P–T–t paths of lower crustal rocks in asymmetric MiCCs

Natural MiCCs show mostly asymmetric fault tectonics dominated by the major detachment that unroofed the metamorphic core. Similarly, both strain-weakening-present numerical end-members developed migmatites in the footwall of a major low-angle detachment (Fig. 5). The similarities in terms of crustal surface geometry encouraged us to look for another practical geological criterion discriminating the two genetically distinct MiCCs. Expecting different thermal histories for the core migmatites and the respective metamorphic carapace, we studied their *P*–*T*–time paths, which were obtained with particle-markers that stored the P–T conditions during the numerical time-steps and became exposed along the detachments. (i) Migmatites formed in an *asthenospheric-heat induced MiCC* (dark green circle,

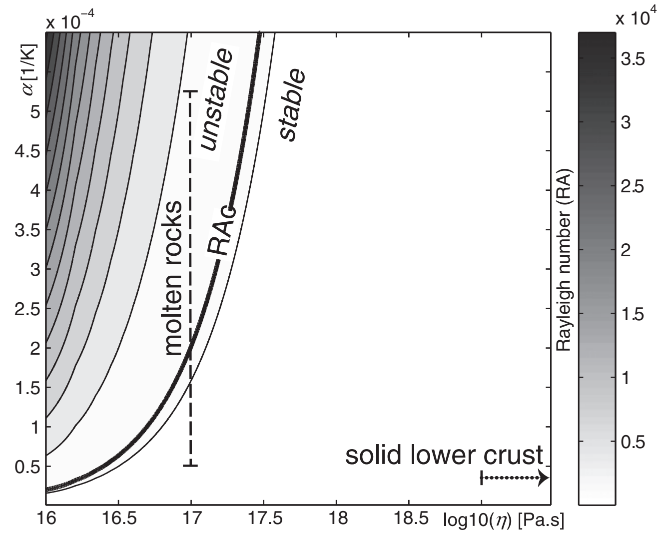

Fig. 4. Rayleigh number (RA) as a function of viscosity η and effective thermal expansion α. For RA > RAc (critical Rayleigh number marking the onset of convections) the layer becomes convective. The dashed-line defines the range of parameters computed in the convective layer of numerical simulations. The dotted line refers to values of the solid lower crust.

Fig. 7a) experienced heating with a minor change in pressure for ca. 8 m-Ma, until peak conditions (T = 750 °C and P = 0.8 GPa). During heating, the rock crossed the solidus before the kyanite–sillimate reaction at 0.8 GPa. After the peak conditions, the rock decompressed during cooling for about 1.1 Ma in the suprasolidus, crossing back into the solidus at pressures of ca. 0.4 GPa at 9.2 m-Ma (Fig. 7c). Final exhumation to the surface lasted ca. 2 m-Ma, passing through the sillimanite–andalusite reaction. The footwall-rocks that were at the lower/upper crust interface (green square) underwent decompressional heating for ca. 6 m-Ma to metamorphic conditions of T = 410 °C and $P \approx 0.4$ GPa before being decompressed and cooled down to exposure. These two dome rocks show therefore different thermal histories before exposure along the detachment. After the first 4.1 m-Ma, during which the green square and circle rock-markers (Fig. 7) had an almost parallel gentle decompression-heating path, the deeper rock (circle) underwent isobaric heating, while the middle crustal rock (square) continued to be decompressed. Peak conditions of the deeper rock were achieved when the mid-crustal rock was already near the surface. This decoupling between the two P–T–time histories reflected the mechanical history of the rocks. The deeper rocks (circle) were heated to melting conditions above the upwelled asthenosphere and laterally displaced in the footwall due to isostatic pressure gradient; meanwhile, the mid-crustal rocks (square) were exhumed along the detachment.

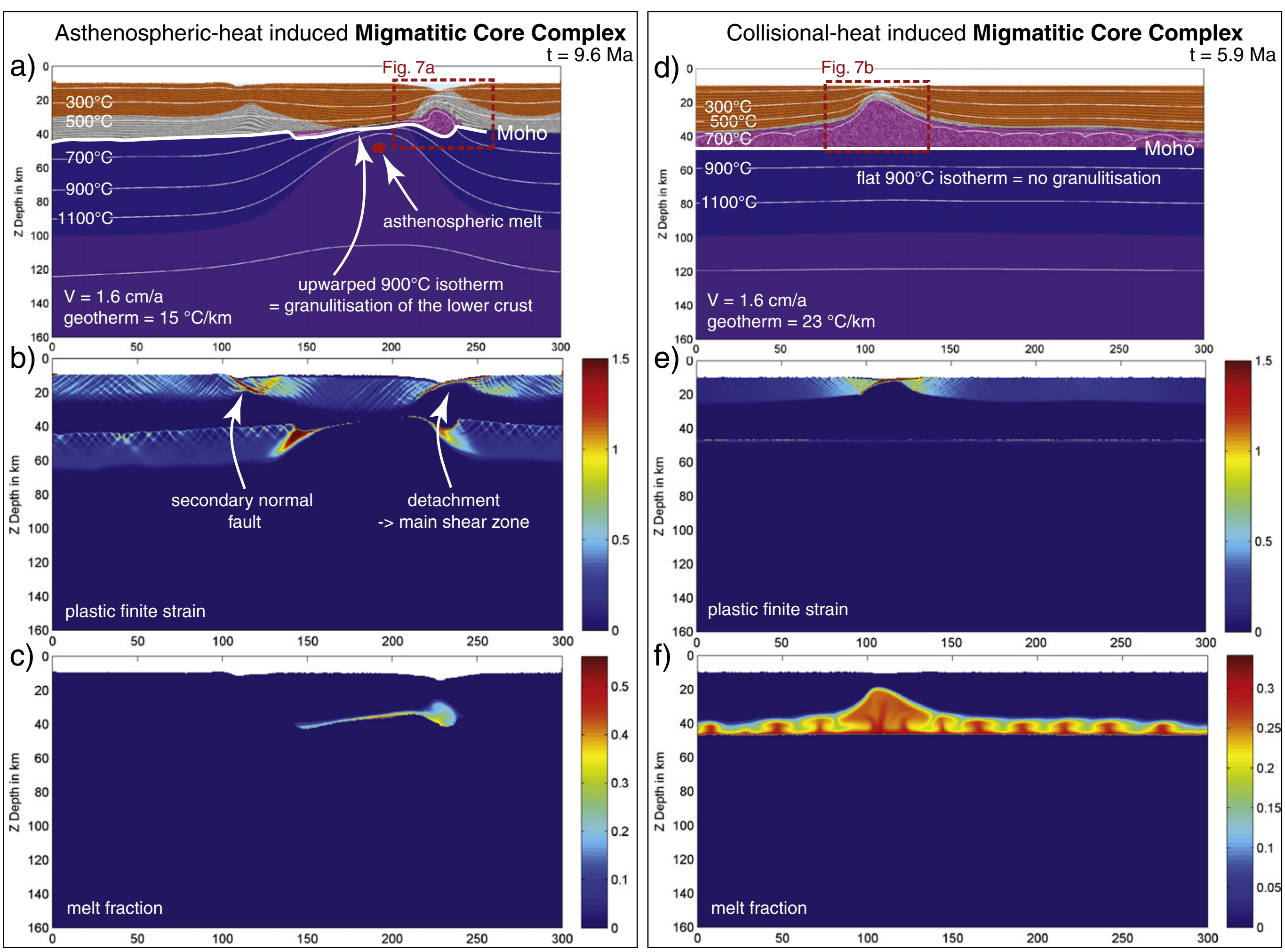

Fig. 5. Rock type (a, d), plastic finite strain (b, e) and melt fraction (c, f) for the two genetic migmatitic core complexes obtained from the two initial end-member thermal conditions: T_{MOHO} = 500 °C and h_0 = 50 km (asthenospheric-heat induced MiCC) and T_{MOHO} = 800 °C and h_0 = 50 km (collisional-heat induced MiCC). Zoom of dashed frames is shown in Fig. 7.

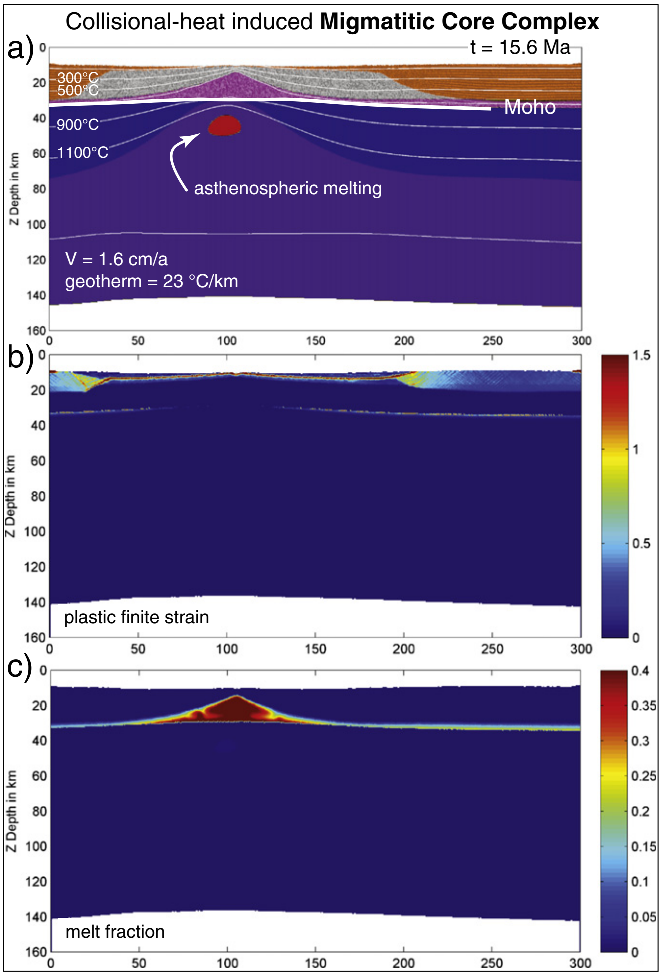

Fig. 6. Rock type (a), plastic finite strain (b) and melt fraction (c) from a collisional heat induced MiCC (same experiment as Fig. 5b but at 15.6 m-Ma, $T_{MOHO}=500$ °C and $h_0=$ 50 km). Snapshot chosen at the time of asthenospheric melting. Note that differently to asthenospheric heat induced MiCC (Fig. 5a) the asthenospheric advection occurred below the MiCC.

(ii) Partially molten rocks (red circle, Fig. 7b) forming *collisional-heat-induced MiCC* first show a short (1 Ma) isothermal increase in pressure, due to convection in the migmatitic layer, then isothermal decompression at peak temperature ($T=750$ °C) for ca. 5 m-Ma (Fig. 7c). The rock marker started in the subsolidus. During decompression, it passed from the kyanite into the sillimanite stability-field at ca. 0.9 GPa, at 4.4 m-Ma. The migmatites crystallized in the subsolidus at ca. 0.3 GPa. At 5.6 m-Ma, the crystallized migmatites entered in the andalusite stability field at ca. 0.2 GPa. The marker starting between the lower and upper crust (red square) showed a one-stage decompressional history with heating during ca. 3 Ma, followed by cooling. The low-grade rock (square) entered into the sillimanite stability field at lower P (ca. 0.6 GPa) and left it at higher P (ca. 0.3 GPa) than the high grade rock (circle). Thus, these two footwall rocks with different metamorphic grades were exhumed following almost parallel *P–T*–time paths shifted by different *T*.

4. Discussion

4.1. Large-scale geometry and fault tectonics: comparing rifting and lower-crustal-doming extensional mode

Rifting and lower-crustal-doming extensional modes (the two end-members without strain softening, Fig. 2) differ substantially in deformation history and final geometry. Cardinal for this study is that rifting models starting from $T_{MOHO}<700$ °C and an initially normal to slightly thickened crust (35 km$<h_0\leq$50 km) do not generate migmatitic domes. $T_{MOHO}>700$ °C and/or initial thick crust $h_0>60$ km are prerequisites to produce MiCCs. The two extensional modes can be qualitatively compared with the "narrow rift mode" and the "metamorphic core complex mode", respectively, of the thin sheet approximation of Buck (1991). However, this does not imply high thermal conditions, since lower crustal doming can also occur with $T_{MOHO}=$ 700 °C and $h_0=70$ km. The resulting initial geotherm of 10 °C/km is consistent with the estimated thermal gradient of cold, thickened orogenic crusts (Lachenbruch and Sass, 1978).

A detailed comparison shows that the rifting mode exhibits a complex, protracted history of crustal faulting and basin development. Early conjugate crustal faults rooting in the Moho-depression (Fig. 3a, $t=6.5$ Ma) create two, ca. 90 km apart basins on the hanging-wall of the shear zones. Later asthenospheric upwelling triggers a new basin between the two former shear zones (Fig. 3a, $t=10.2$). In contrast, in the lower-crustal-doming extensional mode, the upper crust deforms continuously above the migmatitic dome and a single basin is formed (Fig. 3b, $t=3.9$ Ma). The asthenospheric upwelling subsided the basin without delocalizing it, as the asthenosphere is upwelling along the same vertical axis as the migmatitic dome (Fig. 3b, $t=12.3$ Ma). This different faulting behavior results from the rheological stratification (e.g. Gueydan et al., 2008; Tirel et al., 2009). In the rifting mode, the plasticity of the upper mantle favors vertical isostatic compensation (Allemand and Brun, 1991; Brun, 1999; Frederiksen and Braun, 2001; Nagel and Buck, 2004). The resulting offsets in Moho topography control the first stages of crustal deformation. On the contrary, the hot Moho-conditions of the lower-crustal-doming extensional mode induce viscous flow of both lower crust and mantle, maintaining the Moho flat. The pressure gradient between inside and outside the rifted area is compensated by lateral movements of lower crust and mantle material (Block and Royden, 1990). Deformation of the upper plastic crust is consequently not affected by mantle deformation. Thus, the upper crust exhibits a less complex faulting pattern.

Seismic evidence also provides additional discrimination criteria. A flat Moho is only observed in the simulations starting from a hot or deep Moho. These simulations may explain seismic observations in wide extended regions like the Basin and Range (e.g. Hauge et al., 1986) and the Aegean (e.g. Makris and Stobbe, 1984) that are characterized by migmatitic domes, a flat Moho and no remarkable subsidence.

4.2. MiCC thermal history and related heat source

Simulations incorporating strain-softening demonstrate that MiCC can form with an initially low Moho temperature ($T_{Moho}<700$ °C) and intermediate initial crustal thicknesses (35 km$<h_0\leq$50 km), disagreeing with Tirel et al. (2008) who postulated hot conditions ($T_{Moho}>800$ °C) for the formation of metamorphic domes. Huet et al. (2011), simulating the extension of a strong thrusted mafic pile on top of a weaker lower crust, also predicted metamorphic core complexes starting from a cold lithosphere with an inverted lithological stratification.

Depending on the heat source, we distinguished between (i) an asthenospheric-heat and (ii) a collision-heat induced MiCC. The migmatites of these genetically distinct MiCCs show contrasting *P–T*–time loops (Fig. 7c). In natural MiCCs, the high-temperature (HT), intermediate-pressure (IP) metamorphic carapace preserves relicts of low-temperature (LT), high-pressure (HP) metamorphism (e.g. Wijbrans and McDougall, 1986). The petrologic data connect the HP with the HT event either with a "classical" prograde one-stage *P–T* loop (e.g. Duchene et al., 2006) or with a two stage *P–T*–time loop involving early decompression of HP rocks, followed by isobaric heating to peak metamorphic conditions (e.g. Parra et al., 2002). The latter thermal history finds less agreement in the literature because it suggests conductive

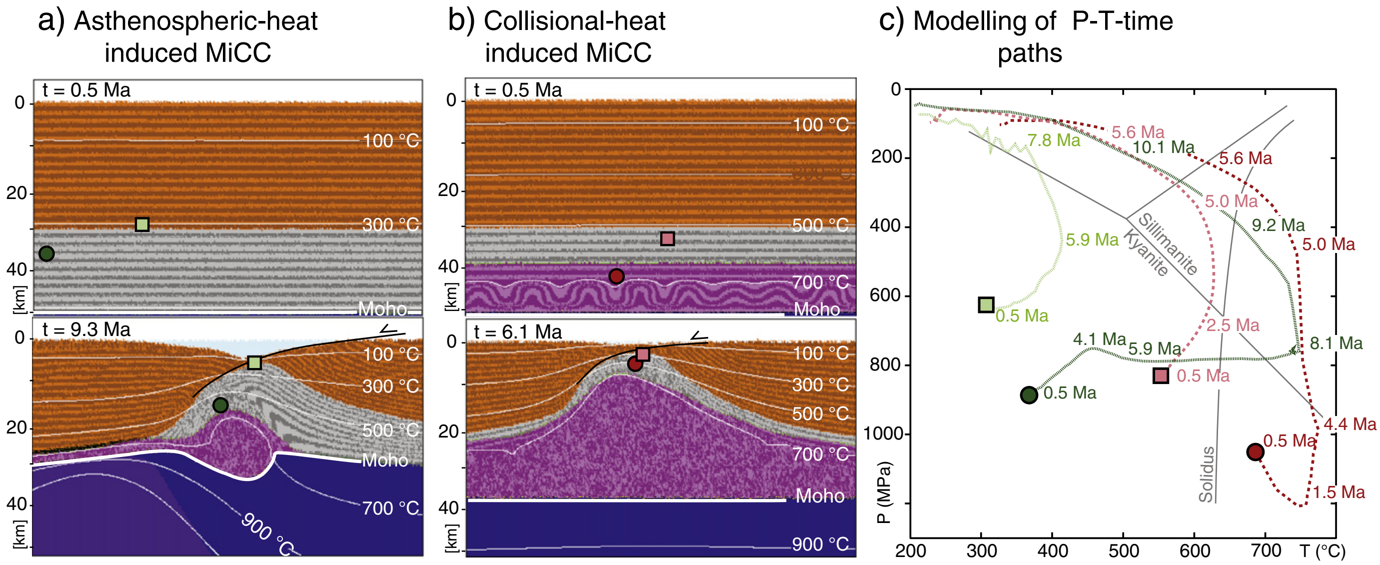

Fig. 7. Migmatitic core complexes zoomed in the areas framed in Fig. 5. a) asthenospheric-heat-induced MiCC with positioned markers. b) collisional-heat-induced MiCC with positioned markers. c) *P–T*-time paths of the markers shown in a) (green) and b) (red). Note that the snapshots (t = 9.3 Ma for a) and t = 6.1 Ma for b)) are taken when the circle markers that experienced partial melting have just been recrystallized.

heat transport that has far too long length and time scales (>50 Ma (England and Thompson, 1984)) with respect to the geological timescales of regional metamorphism (e.g. Oliver et al., 2000). The initial thermal conditions imposed in our numerical setup reflect the thermal content after crustal thickening (the HP event). Therefore, the numerically modeled *P-T*-time trajectories simulate the petrologic *P–T*–time path after the onset of extension. Our results show that the migmatites of a collision-heat induced MiCC follow isothermal decompression from peak conditions during doming (Fig. 5b, c) like the "classical" petrologic prograde one-stage thermal history (Thompson and England, 1984). On the contrary, the migmatite core of asthenospheric-heat induced MiCC experienced isobaric heating at IP to peak conditions in realistic time scale (ca. 8 m-Ma) due to a combination of conductive heating at the bottom of the crust and advective lateral migration of the migmatites in the exhuming footwall. Therefore, both petrological *P–T* paths have thermo-mechanical validity in appropriate geological timescale.

4.3. Convection cells and the role of active (buoyancy) vs. passive (isostasy) doming

The onset of isostatic instabilities and therefore convection cells in the partially molten layer is due to a drop in viscosity combined with an increase in effective thermal expansion of the molten rocks (Fig. 5); the latter term decreases the density of the rock with increasing temperature and melt fraction (see Eq. (A.27) in the Appendix A.3), creating buoyancy. This body force (internal to the system) acts with the external divergent force (velocity imposed at the lateral boundaries) as a driving force for lower crustal doming. The respective role of these driving forces is a debate with long-standing disagreements between "diapirist" and "metamorphic core complex" theories that are summarized in Whitney et al. (2004a).

In our models, the cuspate-lobate shape of the base of the plastic upper crust is not a deep, geometrical effect of upper crustal faults. The structural pattern and the 700 °C-isotherm (Fig. 3b, t = 3.1 Ma) place lobes above migmatite upstreams and cusps where convective migmatite flow downward, in consistency with Rayleigh–Taylor convections. Nevertheless, this buoyancy driven instabilities are not involved in the dome initiation, since the wavelength of the cusps and lobes before doming is smaller than the width of the dome when it begins to amplify (Fig. 3b, t = 3.1 Ma and t = 3.9 Ma). This observation corroborates recent work attesting a combination of isostasy- and buoyancy-flow for the formation of the Naxos dome (Kruckenberg et al., 2011), where the buoyancy-flow is responsible for internal subdomes (the cuspate-lobate architecture in our 2D simulations) in the migmatitic core (Rey et al., 2011). A quantitative analysis of the relative influence of the two dome-driving forces needs numerical codes simulating melt/solid segregation that may enhance active, diapirism-triggered doming by density differences between buoyant leucocratic neosomes and denser refractory restites.

5. Application to natural MiCC

5.1. Eocene Rhodope extension: an asthenosphere-triggered extensional system

The Rhodope results from late Cretaceous to early Tertiary convergence and collision of a continental promontory (Adria–Apulia) to the S with the Moesian platform (Eurasia) to the N (e.g. Dercourt et al., 1986; Dixon and Robertson, 1984). The metamorphic rocks were brought to the surface and unconformably covered with sediments during Maastrichtian-Paleocene time (Boyanov et al., 1982; Goranov and Atanasov, 1992). An Eocene–Oligocene extensional event developed grabens, metamorphic domes and voluminous magmatism and volcanism (e.g. Burg, 2011). In northern Rhodope, four aligned metamorphic domes trending NW–SE were exhumed along low-angle detachments (Fig. 8a). The three western domes expose migmatites. 30 km to the southwest of these structural highs, a voluminous composite pluton (ca. 200 × 20 km) elongated roughly parallel to the domes, intruded the older thrust units in the hanging-walls of the dome-related detachments. The early- to mid-Tertiary granitoids are mostly calc-alkaline and associated with deep crustal melts (Jones et al., 1992). Sm–Nd isotope geochemistry shows a mixed mantle and deep crustal source signature (vonQuadt and Peytcheva, 2005) suggesting that the upwelling of the asthenosphere produced mantle melt and transferred heat to the surroundings for crustal and mantle dehydration melting (Pe-Piper and Piper, 2006). Miocene extension produced a later generation of grabens and detachment. This latter extension was

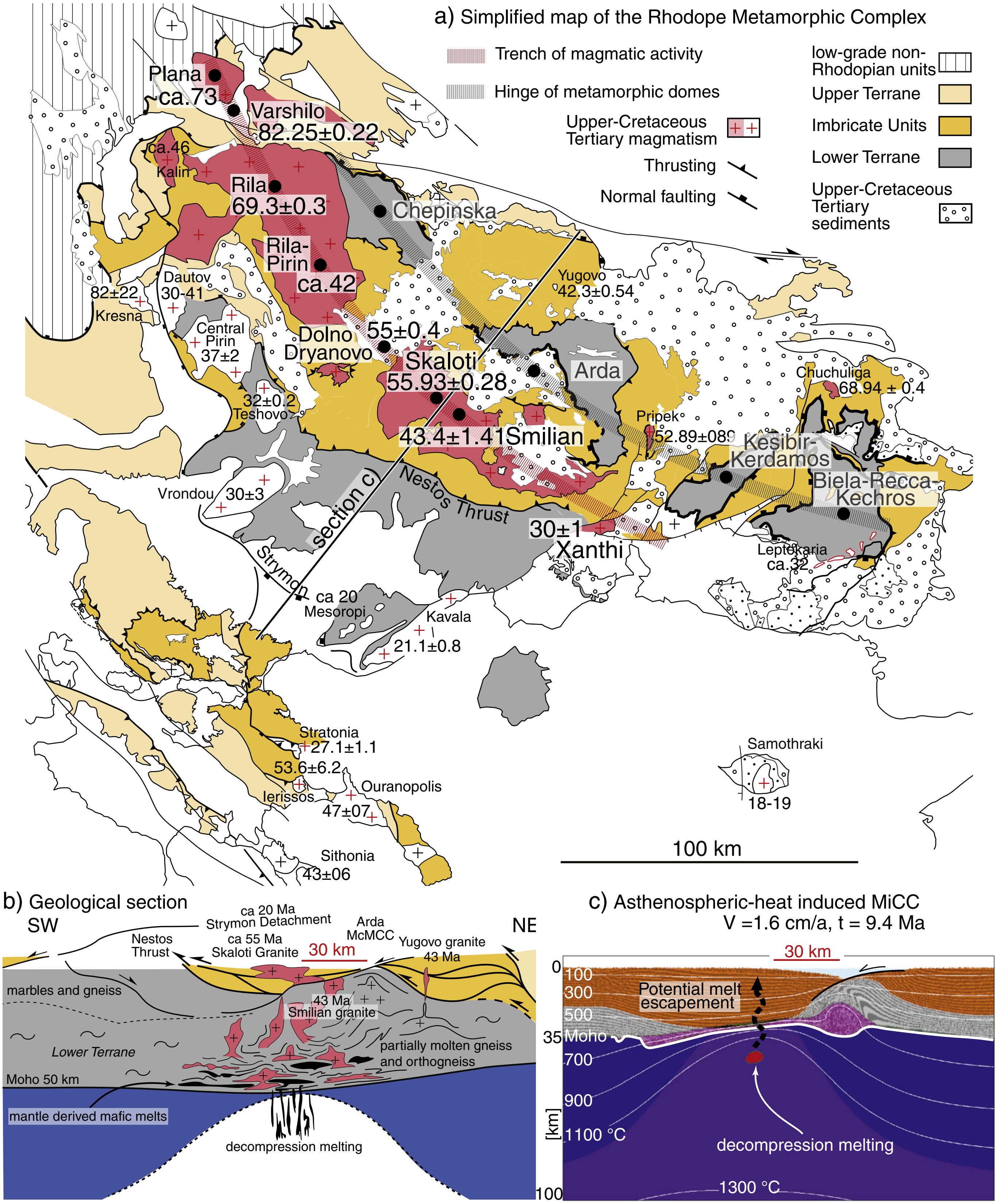

Fig. 8. (a) Sketch map and ages of the plutons reviewed in Burg (2011) (b) section of the Rhodope Metamorphic Complex and (c) simulation with $T_{MOHO} = 500$ °C and $h_0 = 50$ km.

also characterized by magmatic activity, but Miocene plutons (e.g. Kavala granite (Dinter et al., 1995)) intruded in the footwall of the related low-angle (Strymon) detachment.

The experiments of the extension of cold and moderately thick crust match the magmatic activity coeval with the formation of MiCCs, the crustal geometry and the genetic mantle affinity of the

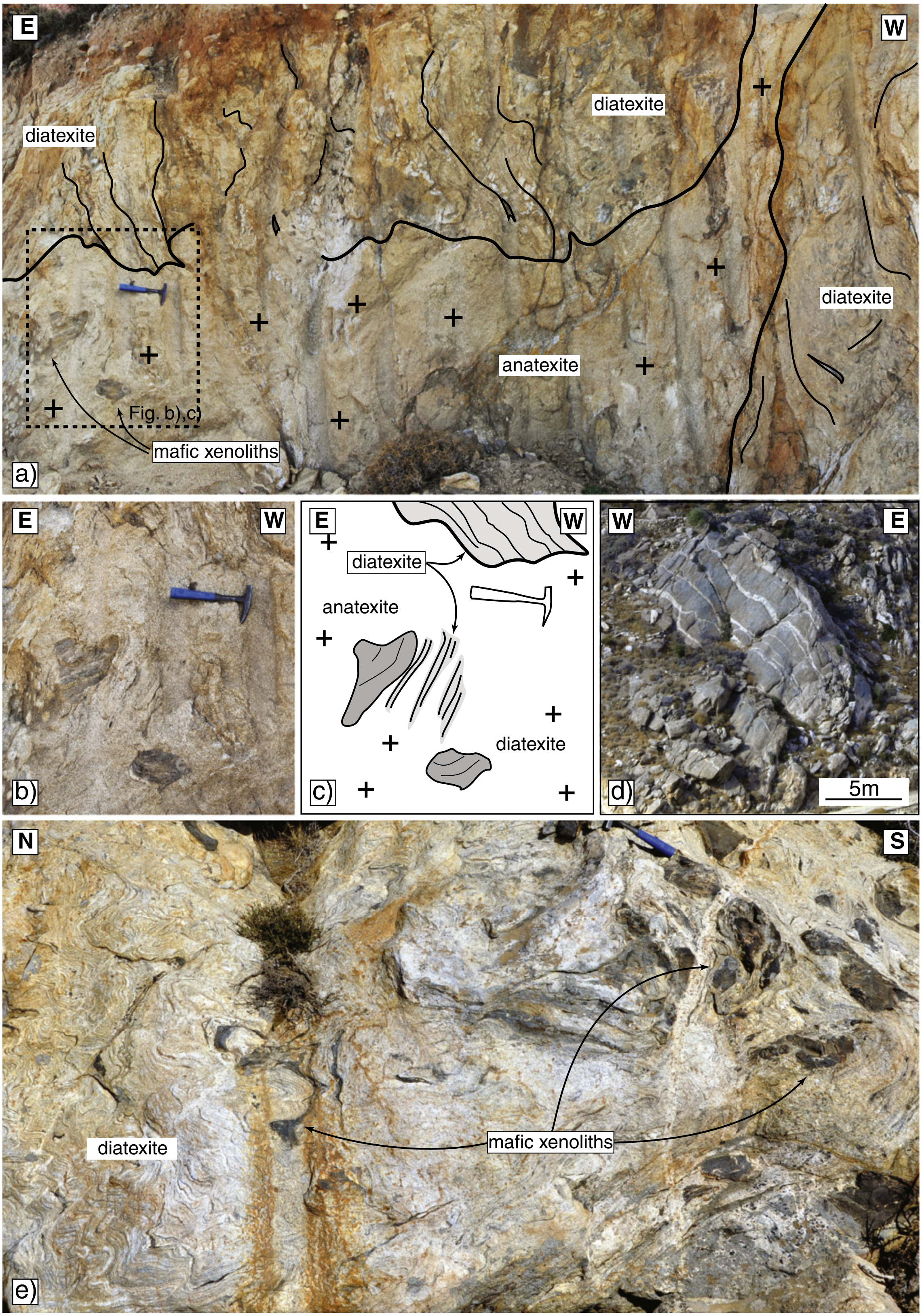

Fig. 9. Naxos migmatites. a) Diatexites intruded by a leucogranite (anatexite) (Coord. 37° 06′ 37.4″ N, 025° 28′ 22.3′ E). b) and c) Textural relationships between diatexites, anatexites (leucogranite) and mafic restitic enclaves. Note that the leucogranite contains fragments that escaped full anatexis. d) Dikes crosscutting the dome (37° 06′ 50.0″ N, 025° 28′ 11.5″ E) e) Folds with curvilinear axes reflecting chaotic flow pattern of the migmatites whose foliation warped passively around stronger xenoliths. (37° 06′ 38.1″ N, 025° 28′ 19.7″ E).

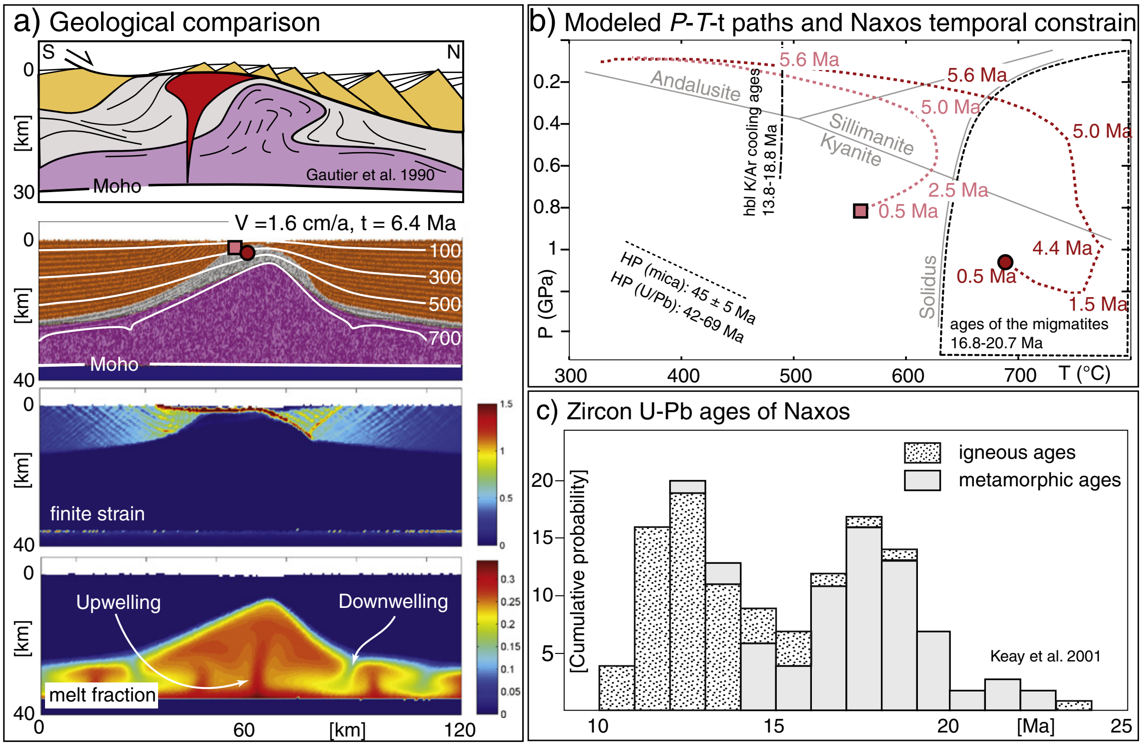

Fig. 10. Numerical visualizations and thermal and temporal constraints of the Naxos dome. a) Geological section from Gautier et al. (1990) compared with the numerical simulation of phases, finite plastic strain and melt fraction. The detachment geometry and the size of the migmatitic core are similar. The melt-fraction visualization allows recognition of up-welling and down-welling channels of the crustal convections. b) Modeled *P–T*-time paths and Naxos thermochronological constraints. Ages of the migmatites (Keay et al., 2001), of the hornblende "hbl" K/Ar cooling ages of the core rocks and of the white micas "HP (mica)" Ar/Ar, K/Ar and Rb–Sr ages (Andriessen et al., 1979), ages on zircons metamorphic overgrows "HP (U/Pb)" (Martin et al., 2006). c) Distribution of zircon U–Pb ages of metamorphites and igneous rocks (Keay et al., 2001).

plutons in the Rhodope complex. It is reasonable to assume that melt produced in the decompressed asthenosphere (Fig. 8c) escapes the system upwards after differentiation in the lower crust, forming plutons at shallow levels. In such a case, plutonism is located in the hanging-walls of detachments bounding the MiCCs, at approximately 30 km from the migmatite domes, as pointed out in the Rhodope case (Fig. 8b). Crustal melting is expected to inherit some mantle signature because of interactions with asthenospheric melts. The plutons that deviate from the magmatic axis (e.g. the Rila granitic complex cutting the Chepinska dome, the Yugovo and the Pripek granites, Fig. 8a) reflect the complexity of an extended viscous lower crust, triggering lateral variations in mixing of crustal and mantle melts, local anatexis and lower crustal flow.

Palinspastic reconstructions and field observations identified several hundreds of km of extension (e.g. 120 km only for the Kerdilion detachment (Brun and Sokoutis, 2007)), suggesting significant crustal thinning in the Rhodope. Controversially, seismic data show an undulated reflective Moho at ca. 50 km depth (Boykova, 1999). Our results suggest that melt produced during asthenospheric upwelling can deliver magma to the crust, minimizing the amount of crustal thinning during extension. Furthermore, we suggest that plutons intruded during Eocene–Oligocene extension along the NW–SE elongated magmatic system strengthened the crust after crystallization (Vigneresse et al., 1996), delocalizing the Miocene extension from the Central Rhodope dome system to the Strymon detachment, further SW.

5.2. The Naxos MiCC heat history and prediction of lower crustal convection cells

The Aegean has undergone convergence between Africa and Eurasia in the same supra-subduction system as the Rhodope in Eocene times. Blueschists and eclogites (up to 20 kbar, Trotet et al., 2001) in the Aegean argue for an early Tertiary cold thick crust, assuming conversion of metamorphic pressure to depth >60 km. Since at least the Oligocene-Miocene boundary, continental extension has been accommodated by low angle-faults that have uncovered metamorphic and structural domes such as the Naxos MiCC (Gautier and Brun, 1994a; Jansen and Schuiling, 1976; Seward et al., 2009; Vanderhaeghe, 2004). The Naxos core rocks have experienced LT–HP (55–40 Ma (Avigad, 1998; Wijbrans and McDougall, 1986) followed by HT–IP (21–12 Ma (Andriessen et al., 1979; Keay et al., 2001; Martin et al., 2006; Wijbrans and McDougall, 1986)) metamorphisms, the latter thermal event being contemporaneous with extension (Buick, 1991; Gautier and Brun, 1994b; Lister et al., 1984). A granodiorite, too small to have affected the regional thermal budget (Jansen and Schuiling, 1976), intruded to the west of the metamorphic dome at 12 Ma (Keay et al., 2001). The core migmatites are situated in the topographic high of the dome and extend for ca. 12×5 km, with the long axis trending NNE.

Our simulations of collisional-heat induced MiCC (T_{MOHO}>700 °C and/or h_0>60 km) fit four interpretations of the Naxos MiCC, stemming from different disciplines: (i) *Flat Moho at shallow depth.* Seismic studies show that the lithospheric structure in the central Aegean is characterized by a flat Moho at 25–28 km depth (Makris and Stobbe, 1984). The Moho cutting the collisional-lithological boundaries observed and projected from the surface obviously developed during post-collisional extension. (ii) *Approximation of Naxos migmatite-magmatic core as a unique viscous body*. Structural and geological field mapping display a migmatitic-magmatic core unroofed below a low angle detachment (Gautier et al., 1990; Kruckenberg et al., 2010; Vanderhaeghe, 2004). The migmatites show a gradient in modal amount of melt, from metatexites in the external envelope to diatexites and leucogranites in the internal part. Migmatites display locally up to 30% melt fraction (Fig. 9), comparable to the amount simulated in numerical experiments (Fig. 10a). A leucogranitic body that intruded discordantly the diatexitic country rock shows, depending on the scale of observation, diffuse margins (Fig. 9a), hinting that diatexites were locally partially molten during intrusion of anatexite. Diatexite clusters included in the same leucogranite (Fig. 9b, c) resisted full recrystallization, suggesting that the melt derived from the same type of gneisses that host the leucogranite (PePiper et al., 1997). Even though melt locally escaped in dikes across the dome (Fig. 9d), the textural relationships testify a bulk viscous deformation of the core rocks. The viscous regime is confirmed by a diffuse seismic anisotropy in the lower lithospheric level of the today rigid block of the central Aegean (e.g. McClusky et al., 2000). This seismic anisotropy trends parallel to the Miocene extension, recording a fossil fabric formed during regional-scale viscous flow (Endrun et al., 2011). (iii) *10–15 Ma of high temperature thermal history and fast cooling of core rocks*. Zircon U–Pb ages of metamorphic rims scatter between 23 and 13 Ma with a peak at 20 Ma whereas the leucogranites ages spread from 20 to 10 Ma with a peak at 13 Ma (Keay et al., 2001) (Fig. 10c). The HT thermal history falls in the same temporal range as the time that the numerical rock markers spend in the supra-solidus range (Fig. 10b). The overlapping of the U/Pb-ages with the K/Ar-ages on hornblende (Andriessen et al., 1979) expresses fast cooling of the metamorphic dome as in the modeled core rocks. (iv) *High temperature at intermediate pressure for the core rocks*. The coexistence of sillimanite–kyanite–andalusite and sillimanite–andalusite in pelites on the western flank of the dome (Jansen and Schuiling, 1976) is convincing evidence that the Naxos core was still hot at IP ($P<400$ MPa at $T>500$ °C). Core peak temperature reached 600–670 °C at pressure between 400 and 800 MPa (Buick and Holland, 1991). The modeled *P–T*–time trajectories pass through the thermal peak condition at IP and enter in the andalusite stability field below the triple point andalusite–sillimanite–kyanite. Furthermore, the trajectories of the core rocks are cooling down at lower *P* than that of the flanks (Fig. 10b), confirming the decrease of *P* from the carapace to the core at peak condition (Duchene et al., 2006).

6. Conclusion

We studied the effects of collisional thermal-heritage (by changing thermal gradient and thickness of the lithosphere) on the extension of a five layer setup (atmosphere, upper crust, lower crust, lithospheric and asthenospheric mantle) with particular attention to MiCC formation and heat source of migmatization.

A first set of experiments testified a bimodal behavior of the lithosphere with a rifting mode for initial $T_{MOHO}<700$ °C and $35<h_0\leq 50$ km and lower-crustal-doming mode with initial $T_{MOHO}>$ 700 °C and/or $h_0>60$ km. In the latter case MiCCs are accompanied by a flat Moho similar to seismic images of the Basin and Range and the Aegean. However, this crustal geometry is not peculiar to an extended hot crust; it can also develop from a 70 km thick orogenic crust with a geotherm of 10 °C/km (alike the Andes).

A second set of experiments incorporating strain-softening of crustal rocks shows the same initial lithospheric-scale bimodal behavior. However, further extension of both modes develops geometrically similar MiCCs roofed by low-angle detachments but different heat sources trigger the different MiCCs. We identified time, structural, petrological and thermal constraints to assess the role of the distinct partial melting heat sources. Asthenospheric-heat induced MiCCs ($T_{MOHO}<700$ °C and $35<h_0\leq 50$ km) show early rift tectonics, during which the asthenosphere rises. Subsequently, (i) migmatization and (ii) UHT (granulite facies) conditions of the lower crust, (iii) migmatitic doming and (iv) mantle melting dislocated by about 30 km with respect to the MiCC take place in a short temporal range (from ca. 5 to 9.5 model-Ma). The migmatitic core rocks experienced isobaric heating to migmatization at intermediate pressure, coeval to the exhumation and cooling of the carapace rocks. Thus, migmatitic core and metamorphic carapace exposed along the detachment have a strongly decoupled thermal history. An example of asthenosphere derived MiCC is recognized in the Eocene Rhodope Migmatitic Dome Complex. Collisional-heat induced MiCCs ($T_{MOHO}>700$ °C and/or $h_0>60$ km) exhibit (i) migmatization that precedes extension and (ii) lower crustal doming paired with a flat Moho. The asthenosphere upwelling with the related (iii) lower crustal UHT metamorphism and (iv) mantle melt take place late after doming below the axis of the migmatitic dome. Therefore, UHT metamorphism and extensional mantle melt are not expected in MiCCs formed in short extensional pulses ($t<12$ Model Ma). The *P–T*–time path of the migmatitic core shows an isothermal decompression in the supra-solidus regime contemporaneously with doming. The latter characteristics are applicable to the Miocene Naxos dome. The migmatitic core of both end-members developed convection cells, whose importance as a buoyant driving force in exhuming the dome remains unsolved. The modeling we have carried out shows further support to integrated and detailed structural/petrological/geochronological studies to specify the geodynamic setting of otherwise geometrically similar structures as metamorphic core complexes.

Acknowledgements

This work was supported by ETH Research Grant ETH-09 09-3. We are thankful to S.M. Lechmann for comments and improvements of the manuscript and to B.J.P. Kaus for discussions. We thank O. Vanderhaeghe and F. Gueydan for their constructive reviews.

Appendix A. Numerical solution of governing equations

The momentum, mass and heat conservation equations for multiphase viscoelastoplastic flow (Gerya, 2010; Gerya and Yuen, 2007) are solved on the non-deforming Eulerian grid whereas the advection of transport properties including viscosity, plastic strain, temperature etc. is performed with the moving Lagrangian markers (Gerya, 2010; Gerya and Yuen, 2007). Notations and the material properties used in the 2D numerical simulations are listed in Tables 1 and 2, respectively.

A.1. Conservation equations and numerical implementation

We have considered 2D creeping flow wherein both thermal and chemical buoyant forces are included, along with heating from adiabatic compression and viscous dissipation in the heat conservation equation.

We have adopted a Lagrangian frame in which the heat conservation equation with thermal conductivity *k* (T, P, C) (Table 2) depending on rock composition (*C*), pressure and temperature takes the form:

$$\rho Cp\left(\frac{DT}{Dt}\right) = -\frac{\partial q_x}{\partial x} - \frac{\partial q_z}{\partial z} + H_r + H_a + H_s \tag{A.1}$$

$$H_a = T\alpha\left(v_x\frac{\partial P}{\partial x} + v_z\frac{\partial P}{\partial z}\right) \tag{A.2}$$

$$H_s = \sigma_{xx}\left(\dot{\varepsilon}_{xx} - \dot{\varepsilon}_{xx(\text{elastic})}\right) + \sigma_{zz}\left(\dot{\varepsilon}_{zz} - \dot{\varepsilon}_{zz(\text{elastic})}\right) + 2\sigma_{xz}\left(\dot{\varepsilon}_{xz} - \dot{\varepsilon}_{xz(\text{elastic})}\right) \tag{A.3}$$

$$q_x = -k(T,P,C)\frac{\partial T}{\partial x} \tag{A.4}$$

$$q_z = -k(T,P,C)\frac{\partial T}{\partial z} \tag{A.5}$$

where DT/Dt represents the substantive time derivative, H_r is the radioactive heating that depends on rock composition (Table 2), and other notations are given in Table 1.

The conservation of mass is approximated by the incompressible continuity equation (Turcotte and Schubert, 2002):

$$\frac{\partial v_x}{\partial x} + \frac{\partial v_z}{\partial z} = 0 \tag{A.6}$$

The 2D Stokes equations for creeping flow take the form:

$$\frac{\partial \sigma_{xx}}{\partial x} + \frac{\partial \sigma_{zz}}{\partial z} = \frac{\partial P}{\partial x} \tag{A.7}$$

$$\frac{\partial \sigma_{zz}}{\partial x} + \frac{\partial \sigma_{xz}}{\partial x} = \frac{\partial P}{\partial z} - g\rho(T, P, C, M) \tag{A.8}$$

The density $\rho(T, P, C, M)$ depends explicitly on temperature, pressure, rock composition and melt fraction. Deviatoric stress components σ_{ij} in Eqs. (A.7) and (A.8) are formulated from visco-elasto-plastic constitutive relationships (Eq. (A.11)) by using first-order finite differences in time $(D\sigma_{ij}/Dt) = (\sigma_{ij} - \sigma^0_{ij})/\Delta t$ in order to represent time derivatives of elastic stresses (Moresi et al., 2003):

$$\sigma_{ij} = 2\eta_{vp}\dot{\varepsilon}_{ij}Z + \sigma^o_{ij}(1-Z) \tag{A.9}$$

$$Z = \frac{\Delta t \mu}{\Delta t \mu + \eta_{vp}} \tag{A.10}$$

$\eta_{vp} = \eta$, when $(\sigma_{II})^{1/2} < \sigma_{\text{yield}}$, and $\eta_{vp} = \eta\frac{(\sigma_{II})^{1/2}}{\eta\chi + (\sigma_{II})^{1/2}}$, when $(\sigma_{II})^{1/2} = \sigma_{\text{yield}}$, in which Δt is elastic time step, σ^0_{ij} is the deviatoric stress tensor from the previous time slice corrected for advection and rotation by using a non-diffusive markerin-cell technique (Gerya and Yuen, 2007; Moresi et al., 2003). Z is the viscoelasticity factor, η is effective viscosity and η_{vp} is a viscosity-like parameter computed iteratively to satisfy the plastic yielding condition ($\eta_{vp} = \eta$, when no plastic yielding occurs).

A.2. Rheological model

The bulk strain rate of the visco-elasto-plastic rheology has been implemented with the respective three components (e.g. Gerya, 2010):

$$\dot{\varepsilon}_{ij} = \dot{\varepsilon}_{ij(\text{viscous})} + \dot{\varepsilon}_{ij(\text{elastic})} + \dot{\varepsilon}_{ij(\text{plastic})} \tag{A.11}$$

Where

$$\dot{\varepsilon}_{ij(\text{viscous})} = \frac{1}{2\eta}\sigma_{ij} \tag{A.12}$$

$$\dot{\varepsilon}_{ij(\text{elastic})} = \frac{1}{2\mu}\frac{D\sigma_{ij}}{Dt} \tag{A.13}$$

$\dot{\varepsilon}_{ij(\text{plastic})} = 0$, when $(\sigma_{II})^{\frac{1}{2}} < \sigma_{\text{yield}}$ and

$$\dot{\varepsilon}_{ij(\text{plastic})} = \chi\frac{\partial G}{\partial \sigma_{ij}} = \chi\frac{\sigma_{ij}}{2\sigma_{II}^{1/2}}, \text{when } (\sigma_{II})^{1/2} = \sigma_{\text{yield}} \tag{A.14}$$

where $D\sigma_{ij}/Dt$ is objective co-rotational time derivative of deviatoric stress component σ_{ij}, σ_{yield} the plastic yield strength for given rock, $G = (\sigma_{II})^{1/2}$ the plastic potential of non-dilatant material, σ_{II} is second deviatoric stress invariant, μ is shear modulus and χ is plastic multiplier satisfying the plastic yielding condition $(\sigma_{II})^{1/2} = \sigma_{\text{yield}}$, where $\sigma_{II} = 1/2\ \sigma_{ij}\ \sigma_{ij}$ is second deviatoric stress invariant. The effective viscosity of solid rocks ($M \le 0.1$) essentially depends on stress, pressure and temperature. It is defined in terms of the second deviatoric stress invariant (Ranalli, 1995) as:

$$\eta = \left(\frac{4}{\sigma_{II}}\right)^{(n-1)/2}\frac{F^n}{A_D}\exp\left(\frac{E+VP}{RT}\right) \tag{A.15}$$

where A_D, E, V and n are experimentally determined flow law parameters (Table 2). F is a dimensionless coefficient depending on the type of experiments on which the flow law is based (Ranalli, 1995). For example:

$$F = \frac{2^{(1-n)/n}}{3^{(1+n)/2n}}, \text{for triaxial compression and} \tag{A.16}$$

$$F = 2^{(1-2n)/n}, \text{for simple shear.} \tag{A.17}$$

10^{17} and 10^{26} Pa s are respectively the lower and upper cutoff limits for viscosity of all types of crustal rocks in the presented simulations.

The effect of erosion and sedimentation on the topography is solved with the transport equation applied at the surface (Gorczyk et al., 2007). This equation is solved at each time-step in the Eulerian coordinates:

$$\frac{\partial z_{es}}{\partial t} = v_z - v_x\frac{\partial z_{es}}{\partial x} - v_s + v_e \tag{A.18}$$

Where z_{es} is the vertical position of the surface as a function of the horizontal distance x; v_z and v_x are the vertical and the horizontals components of the material velocity vector at the surface (z is positive downward, $z = 0$ at the top of the box); v_s and v_e are the gross-scale sedimentation and erosion rates respectively. The following values where used $v_s = 0.0$ mm a^{-1} and $v_e = 0.3$ mm a^{-1} for z < 10 km and $v_s = 0.3$ mm a^{-1} and $v_e = 0.0$ mm a^{-1} for z > 10 km. In regions with steep surfaces, for example on fault scarp, an increased erosion/sedimentation rate (1 mm a^{-1}) is used to account for additional mass transport in the regions with steep (>30°) topography slopes.

In extensional domes the deformation is accommodated in the upper crustal domain by fault tectonics, hence plastic deformation plays a significant role during doming. Fluid and melt percolation along forming fracture zones tends to soften the rock and to localize deformation (Lister and Davis, 1989). In order to approximate the softening effect of fluids and grain size reduction during plastic deformation, the plastic yield strength of rocks is defined similar to Huismans et al. (2005):

$$\sigma_{\text{yield}} = c_1 + \sin(F_1), \text{when } \varepsilon_{ij} < \varepsilon_1 \tag{A.19}$$

c_1 linearly changes to c_2 and $\sin(F_1)$ linearly changes to $\sin(F_2)$ from ε_1 to ε_2, and

$$\sigma_{\text{yield}} = c_2 + \sin(F_2), \text{when } \varepsilon_{ij} > \varepsilon_1. \tag{A.20}$$

The parametric study (see chapter 3.1 and 3.2) was performed without strain softening, i.e. with $c_1 = c_2 = 5 \times 10^5$ and $\sin(F_1) = \sin(F_2) = 0.4$. In the runs where we applied strain softening, such values were used: $c_1 = c_2 = 5 \times 10^5$, $\sin(F_1) = 0.5$, $\sin(F_2) = 0.07$, $\varepsilon_1 = 0.5$ and $\varepsilon_2 = 1.5$ for the experiments with $T_{\text{MOHO}} < 700$ °C, and $c_1 = c_2 = 5 \times 10^5$, $\sin(F_1) = 0.2$, $\sin(F_2) = 0.001$, $\varepsilon_1 = 0.5$ and $\varepsilon_2 = 1.5$ for the experiments $T_{\text{MOHO}} > 700$ °C. Lower value for the coefficient of internal friction ($F_{1,2}$) has been chosen in experiments with higher thermal conditions. This simulates the increase of fluid percolation in shear zones at higher temperatures.

The effective viscosity η of molten rocks ($M>0.1$) was set to a lower cutoff viscosity value of 10^{17} Pa s.

A.3. Melt crystallization and partial melting

At constant pressure the volumetric fraction of melt M is assumed to increase linearly with temperature according to the relations (Burg and Gerya, 2005; Gerya and Yuen, 2003):

$$M = 0, \text{at } T \leq T_{\text{solidus}}, \tag{A.21}$$

$$M = \frac{T - T_{\text{solidus}}}{T_{\text{liquidus}} - T_{\text{solidus}}}, \text{at } T_{\text{solidus}} < T < T_{\text{liquidus}}, \tag{A.22}$$

$$M = 1, T \geq T_{\text{liquidus}} \tag{A.23}$$

where T_{solidus} and T_{liquidus} are the wet solidus and dry liquidus temperatures of the considered rock, respectively (Table 2).

The volumetric fraction of melt M influences the effective density, ρ_{eff}, of the partially molten rocks:

$$\rho_{eff} = \rho_{\text{solid}} - M(\rho_{\text{solid}} - \rho_{\text{molten}}) \tag{A.24}$$

where ρ_{solid} and ρ_{molten} are the densities of solid and molten rocks, respectively, which depend on pressure and temperature according to the relation:

$$\rho_{P,T} = \rho_0[1 - \alpha(T - T_0)][1 + \beta(P - P_0)] \tag{A.25}$$

where ρ_0 is the standard density at $P_0 = 0.1$ MPa and $T_0 = 298$ K; α and β are the thermal expansion and compressibility coefficients, respectively.

In the range between $0<M<1$ the effect of latent heating due to equilibrium melting/crystallization is included implicitly by increasing the effective heat capacity (C_{Peff}) and the thermal expansion ($\alpha_{eff} = \alpha_v$), similarly to Burg and Gerya (2005):

$$Cp_{eff} = Cp + Q_L \left(\frac{\partial M}{\partial T}\right)_P \tag{A.26}$$

$$\alpha_{eff} = \alpha + \rho \frac{Q_L}{T} \left(\frac{\partial M}{\partial P}\right)_T \tag{A.27}$$

where Cp is the heat capacity of the solid rock, and Q_L is the latent heat of melting of the rock.

References

Afonso, J.C., Ranalli, G., 2004. Crustal and mantle strengths in continental lithosphere: is the jelly sandwich model obsolete? Tectonophysics 394, 221–232.
Allemand, P., Brun, J.P., 1991. Width of continental rifts and rheological layering of the lithosphere. Tectonophysics 188, 63–69.
Altherr, R., Henjes-Kunst, F., Matthews, A., Friedrichsen, H., Hansen, B.T., 1988. O–Sr Isotopic variations in Miocene granitoids from the aegean: evidence for an origin by combined assimilation and fractional crystallization. Contributions to Mineralogy and Petrology 100, 528–541.
Andersen, T.B., Jamtveit, B., Dewey, J.F., Swensson, E., 1991. Subduction and eduction of continental-crust: major mechanisms during continent-continent collision and orogenic extensional collapse, a model Based on the South Norwegian Caledonides. Terra Nova 3, 303–310.
Andriessen, P.A.M., Boelrijk, N.A.I.M., Hebeda, E.H., Priem, H.N.A., Verdurmen, E.A.T., Verschure, R.H., 1979. Dating the events of metamorphism and granitic magmatism in the Alpine Orogen of Naxos (Cyclades, Greece). Contributions to Mineralogy and Petrology 69, 10.
Artemieva, I.M., Mooney, W.D., 2001. Thermal thickness and evolution of Precambrian lithosphere: a global study. Journal of Geophysical Research, B: Solid Earth 106, 16387–16414.
Avigad, D., 1998. High-pressure metamorphism and cooling on SE Naxos (Cyclades, Greece). European Journal of Mineralogy 10, 1309–1319.
Block, L., Royden, L.H., 1990. Core complex geometries and regional scale flow in the lower crust. Tectonics 9, 557–567.
Bousquet, R., Goffe, B., Henry, P., LePichon, X., Chopin, C., 1997. Kinematic, thermal and petrological model of the Central Alps: lepontine metamorphism in the upper crust and eclogitisation of the lower crust. Tectonophysics 273, 105–127.
Boyanov, I., Ruseva, M., Dimitrova, E., 1982. First find of Upper-Cretaceous foraminifers in the East-Rhodopes. Geologica Balcanica 12, 20–21.
Boykova, A., 1999. Moho discontinuity in Central Balkan Peninsula in the light of the geostatistical structural analysis. Physics of the Earth and Planetary Interiors 114, 49–58.
Briole, P., Rigo, A., Lyon-Caen, H., Ruegg, J.C., Papazissi, K., Mitsakaki, C., Balodimou, A., Veis, G., Hatzfeld, D., Deschamps, A., 2000. Active deformation of the Corinth Rift, Greece: results from repeated global positioning system surveys between 1990 and 1995. Journal of Geophysical Research, B: Solid Earth 105, 25605–25625.
Brun, J.P., 1999. Narrow rifts versus wide rifts: inferences for the mechanics of rifting from laboratory experiments. Philosophical Transactions of the Royal Society of London, Series A 357, 695–710.
Brun, J.P., Sokoutis, D., 2007. Kinematics of the Southern Rhodope Core Complex (North Greece). International Journal of Earth Sciences 96, 1079–1099.
Buck, W.R., 1988. Flexural rotation of normal faults. Tectonics 7, 959–973.
Buck, W.R., 1991. Modes of continental lithospheric extension. Journal of Geophysical Research, B: Solid Earth 96, 20161–20178.
Buick, I.S., 1991. The Late Alpine evolution of an extensional shear zone, Naxos, Greece. Journal of the Geological Society (London, United Kingdom) 148, 93–103.
Buick, I.S., Holland, T.J.B., 1991. The nature and distribution of fluids during amphibolite facies metamorphism, Naxos (Greece). Journal of Metamorphic Geology 9, 301–314.
Buiter, S.J.H., Huismans, R.S., Beaumont, C., 2008. Dissipation analysis as a guide to mode selection during crustal extension and implications for the styles of sedimentary basins. Journal of Geophysical Research, B: Solid Earth 113.
Burg, J.-P., 2011. Rhodope: from Mesozoic convergence to Cenozoic extension. review of petro-structural data in the geochronological frame. Journal of the Virtual Explorer 39, 44.
Burg, J.P., Gerya, T.V., 2005. The role of viscous heating in Barrovian metamorphism of collisional orogens: thermomechanical models and application to the Lepontine Dome in the Central Alps. Journal of Metamorphic Geology 23, 75–95.
Burg, J.P., Vanderhaeghe, O., 1993. Structures and way-up criteria in migmatites, with application to the Velay Dome (French Massif-Central). Journal of Structural Geology 15, 1293–1301.
Burg, J.-P., Van Den Driessche, J., Brun, J.P., 1994. Syn- to post-thickening extension in the Variscan Belt of Western Europe: modes and structural consequences. Géology de la France 3, 18.
Burg, J.P., Nievergelt, P., Oberli, F., Seward, D., Davy, P., Maurin, J.C., Diao, Z.Z., Meier, M., 1998. The Namche Barwa syntaxis: evidence for exhumation related to compressional crustal folding. Journal of Asian Earth Sciences 16, 239–252.
Burov, E., Yamato, P., 2008. Continental plate collision, P–T–t–Z conditions and unstable vs. stable plate dynamics: insights from thermo-mechanical modelling. Lithos 103, 178–204.
Camacho, A., Lee, J.K.W., Hensen, B.J., Braun, J., 2005. Short-Lived orogenic cycles and the eclogitization of cold crust by spasmodic hot fluids. Nature 435, 1191–1196.
Clauser, C., Huenges, E., 1995. Thermal conductivity of rocks, minerals. In: Ahrens, T.J. (Ed.), Rock Physics and Phase Relations. American Geophysical Union, Washington, DC, pp. 105–126.
Davis, G.A., Coney, P.J., 1979. Geologic development of the Cordilleran metamorphic core complexes. Geology 7, 4.
Dercourt, J., Zonenshain, L.P., Ricou, L.E., Kazmin, V.G., Lepichon, X., Knipper, A.L., Grandjacquet, C., Sbortshikov, I.M., Geyssant, J., Lepvrier, C., Pechersky, D.H., Boulin, J., Sibuet, J.C., Savostin, L.A., Sorokhtin, O., Westphal, M., Bazhenov, M.L., Lauer, J.P., Bijuduval, B., 1986. Geological evolution of the Tethys Belt from the Atlantic to the Pamirs since the Lias. Tectonophysics 123, 241–315.
Dinter, D.A., Macfarlane, A., Hames, W., Isachsen, C., Bowring, S., Royden, L., 1995. U–Pb and Ar-40/Ar-39 geochronology of the Symvolon Granodiorite: implications for the thermal and structural evolution of the Rhodope Metamorphic Core Complex, Northeastern Greece. Tectonics 14, 886–908.
Dixon, J.E., Robertson, A.H.F., 1984. The Geological Evolution of the Eastern Mediterranean. Geological Society, London.
Duchene, S., Aissa, R., Vanderhaeghe, O., 2006. Pressure–temperature–time evolution of metamorphic rocks from Naxos (Cyclades, Greece): constraints from thermobarometry and Rb/Sr dating. Geodinamica Acta 19, 301–321.
Echtler, H., Malavieille, J., 1990. Extensional tectonics, basement uplift and Stephano-Permian Collapse Basin in a Late Variscan Metamorphic Core Complex (Montagne Noire, Southern Massif-Central). Tectonophysics 177, 125–138.
Endrun, B., Lebedev, S., Meier, T., Tirel, C., Friederich, W., 2011. Complex layered deformation within the Aegean crust and mantle revealed by seismic anisotropy. Nature Geoscience 4, 203–207.
Engi, M., Berger, A., Roselle, G.T., 2001. Role of the tectonic accretion channel in collisional orogeny. Geology 29, 1143–1146.
England, P.C., Thompson, A.B., 1984. Pressure–temperature–time paths of regional metamorphism 1. Heat transfer during the evolution of regions of thickened continental crust. Journal of Petrology 25, 34.
Faccenda, M., Gerya, T.V., Burlini, L., 2009. Deep slab hydration induced by bending-related variations in tectonic pressure. Nature Geoscience 2, 790–793.
Frederiksen, S., Braun, J., 2001. Numerical modelling of strain localisation during extension of the continental lithosphere. Earth and Planetary Science Letters 188, 241–251.
Gautier, P., Brun, J.P., 1994a. Crustal-scale geometry and kinematics of Late-Orogenic Extension in the Central Aegean (Cyclades and Evvia Island). Tectonophysics 238, 399–424.

Gautier, P., Brun, J.P., 1994b. Ductile crust exhumation and extensional detachments in the Central Aegean (Cyclades and Evvia Islands). Geodinamica Acta 7, 57–85.
Gautier, P., Ballèvre, M., Brun, J.-P., Jolivet, L., 1990. Extension ductile Et Bassins Sédimentaires Mio-Pliocènes Dans Les Cyclades (Îles De Naxos Et Paros). Comptes Rendus de l' Academie des Sciences Paris 310, 7.
Gerya, T., 2010. Introduction to numerical geodynamic modelling.
Gerya, T.V., Burg, J.P., 2007. Intrusion of ultramafic magmatic bodies into the continental crust: numerical simulation. Physics of the Earth and Planetary Interiors 160, 124–142.
Gerya, T.V., Yuen, D.A., 2003. Rayleigh–Taylor instabilities from hydration and melting propel 'cold plumes' at subduction zones. Earth and Planetary Science Letters 212, 47–62.
Gerya, T.V., Yuen, D.A., 2007. Robust characteristics method for modelling multiphase visco-elasto-plastic thermo-mechanical problems. Physics of the Earth and Planetary Interiors 163, 83–105.
Goffe, B., Bousquet, R., Henry, P., Le Pichon, X., 2003. Effect of the chemical composition of the crust on the metamorphic evolution of orogenic wedges. Journal of Metamorphic Geology 21, 123–141.
Goranov, A., Atanasov, G., 1992. Lithostratigraphy and formation conditions of Maastrichtian-Paleocene deposits in Krumovgra District. Geologica Balcanica 22, 11.
Gorczyk, W., Willner, A.P., Gerya, T.V., Connolly, J.A.D., Burg, J.P., 2007. Physical controls of magmatic productivity at Pacific-type convergent margins: numerical modelling. Physics of the Earth and Planetary Interiors 163, 209–232.
Gueydan, F., Morency, C., Brun, J.P., 2008. Continental rifting as a function of lithosphere mantle strength. Tectonophysics 460, 83–93.
Hauge, T.A., Hauser, E.C., Oliver, J.E., Potter, C.J., Klemperer, S., 1986. The Moho in the Northern Basin and Range Province, Nevada, along the Cocorp 40-degree-N seismic-reflection transect. Geological Society of America Bulletin 97, 603–618.
Hawkesworth, C., Turner, S., Gallagher, K., Hunter, A., Bradshaw, T., Rogers, N., 1995. Calc-alkaline magmatism, lithospheric thinning and extension in the basin and range. Journal of Geophysical Research, B: Solid Earth 100, 10271–10286.
Hess, P.C., 1989. Origin of Igneous Rocks. Harward University Press, London.
Huerta, A.D., Royden, L.H., Hodges, K.V., 1998. The thermal structure of collisional orogens as a response to accretion, erosion, and radiogenic heating. Journal of Geophysical Research, B: Solid Earth 103, 15287–15302.
Huet, B., Le Pourhiet, L., Labrousse, L., Burov, E., Jolivet, L., 2011. Post-Orogenic extension and metamorphic core complexes in a heterogeneous crust: the role of crustal layering inherited from collision. Application to the Cyclades (Aegean Domain). Geophysical Journal International 184, 611–625.
Huismans, R., Beaumont, C., 2011. Depth-dependent extension, two-stage breakup and cratonic underplating at rifted margins. Nature 473, 74–U85.
Huismans, R.S., Buiter, S.J.H., Beaumont, C., 2005. Effect of plastic-viscous layering and strain softening on mode selection during lithospheric extension. Journal of Geophysical Research, B: Solid Earth 110, 17.
Jamieson, R.A., Beaumont, C., Fullsack, P., Lee, B., 1998. Barrovian regional metamorphism: where's the heat? Geological Society Special Publication 138, 23–51.
Jansen, J.B.H., Schuiling, R.D., 1976. Metamorphism on Naxos: petrology and geothermal gradients. American Journal of Science 276, 1225–1253.
Jones, C.E., Tarney, J., Baker, J.H., Gerouki, F., 1992. Tertiary granitoids of Rhodope, Northern Greece: magmatism related to extensional collapse of the Hellenic Orogen. Tectonophysics 210, 295–314.
Keay, S., Lister, G., Buick, I., 2001. The timing of partial melting, Barrovian metamorphism and granite intrusion in the Naxos Metamorphic Core Complex, Cyclades, Aegean Sea, Greece. Tectonophysics 342, 37.
Kincaid, C., Silver, P., 1996. The role of viscous dissipation in the Orogenic process. Earth and Planetary Science Letters 142, 271–288.
Kruckenberg, S.C., Ferre, E.C., Teyssier, C., Vanderhaeghe, O., Whitney, D.L., Seaton, N.C.A., Skord, J.A., 2010. Viscoplastic flow in migmatites deduced from Naxos Dome, Greece. Journal of Geophysical Research, B: Solid Earth 115.
Kruckenberg, S.C., Vanderhaeghe, O., Ferre, E.C., Teyssier, C., Whitney, D.L., 2011. Flow of partially molten crust and the internal dynamics of a migmatite dome, Naxos, Greece. Tectonics 30.
Lachenbruch, A.H., Sass, J.H., 1978. Models of an extending lithosphere and heat flow in the basin and range province. In: Smith, R.B., Eaton, G.P. (Eds.), Cenozoic tectonics and regional geophysics of the Western Cordillera: Geol. Soc. Am. Memoir, pp. 221–226.
Ledru, P., Courrioux, G., Dallain, C., Lardeaux, J.M., Montel, J.M., Vanderhaeghe, O., Vitel, G., 2001. The Velay Dome (French Massif Central): melt generation and granite emplacement during Orogenic evolution. Tectonophysics 342, 30.
Lister, G.S., Davis, G.A., 1989. The origin of metamorphic core complexes and detachment faults formed during tertiary continental extension in the Northern Colorado River Region, USA. Journal of Structural Geology 11, 65–94.
Lister, G.S., Banga, G., Feenstra, A., 1984. Metamorphic core complexes of Cordilleran type in the Cyclades, Aegean Sea, Greece. Geology 12, 5.
Makris, J., Stobbe, C., 1984. Physical-properties and state of the crust and upper mantle of the Eastern Mediterranean-Sea deduced from geophysical-data. Marine Geology 55, 347–363.
Martin, L., Duchene, S., Deloule, E., Vanderhaeghe, O., 2006. The isotopic composition of zircon and garnet: a record of the metamorphic history of Naxos, Greece. Lithos 87, 174–192.
McClusky, S., Balassanian, S., Barka, A., Demir, C., Ergintav, S., Georgiev, I., Gurkan, O., Hamburger, M., Hurst, K., Kahle, H., Kastens, K., Kekelidze, G., King, R., Kotzev, V., Lenk, O., Mahmoud, S., Mishin, A., Nadariya, M., Ouzounis, A., Paradissis, D., Peter, Y., Prilepin, M., Reilinger, R., Sanli, I., Seeger, H., Tealeb, A., Toksoz, M.N., Veis, G., 2000. Global positioning system constraints on plate kinematics and dynamics in the Eastern Mediterranean and Caucasus. Journal of Geophysical Research, B: Solid Earth 105, 5695–5719.
Moresi, L., Dufour, F., Muhlhaus, H.B., 2003. A Lagrangian integration point finite element method for large deformation modeling of viscoelastic geomaterials. Journal of Computational Physics 184, 476–497.
Nagel, T.J., Buck, W.R., 2004. Symmetric alternative to asymmetric rifting models. Geology 32, 937–940.
Norton, M.G., 1986. Late Caledonide extension in Western Norway: a response to extreme crustal thickening. Tectonics 5, 195–204.
Oliver, G.J.H., Chen, F., Buchwaldt, R., Hegner, E., 2000. Fast tectonometamorphism and exhumation in the type area of the Barrovian and Buchan Zones. Geology 28, 459–462.
Parra, T., Vidal, O., Jolivet, L., 2002. Relation between the intensity of deformation and retrogression in Blueschist Metapelites of Tinos Island (Greece) evidenced by chlorite-mica local equilibria. Lithos 63, 41–66.
Pe-Piper, G., Piper, D.J.W., 2006. Unique features of the Cenozoic igneous rocks of Greece. Geological Society of America Special Paper 409, 259–281.
PePiper, G., Kotopouli, C.N., Piper, D.J.W., 1997. Granitoid rocks of Naxos, Greece: regional geology and petrology. Geological Journal 32, 153–171.
Ranalli, G., 1995. Rheology of the Earth. Chapman & Hall, London.
Rey, P.F., Teyssier, C., Whitney, D.L., 2009. The role of partial melting and extensional strain rates in the development of metamorphic core complexes. Tectonophysics 477, 135–144.
Rey, P.F., Teyssier, C., Kruckenberg, S.C., Whitney, D.L., 2011. Viscous collision in channel explains double domes in metamorphic core complexes. Geology 39, 387–390.
Rosenberg, C.L., 2001. Deformation of partially molten granite: a review and comparison of experimental and natural case studies. International Journal of Earth Sciences 90, 60–76.
Schmeling, H., Babeyko, A.Y., Enns, A., Faccenna, C., Funiciello, F., Gerya, T., Golabek, G.J., Grigull, S., Kaus, B.J.P., Morra, G., Schmalholz, S.M., van Hunen, J., 2008. A benchmark comparison of spontaneous subduction models-towards a free surface. Physics of the Earth and Planetary Interiors 171, 198–223.
Schmidt, M.W., Poli, S., 1998. Experimentally based water budgets for dehydrating slabs and consequences for arc magma generation. Earth and Planetary Science Letters 163, 361–379.
Seranne, M., Seguret, M., 1987. The Devonian Basins of Western Norway: tectonics and kinematics of an extending crust. In: Coward, M.P., Dewey, J.F., Hancock, P.L. (Eds.), Continental Extensional Tectonics. Geological Society Special Publication, London, p. 9.
Seward, D., Vanderhaeghe, O., Siebenaller, L., Thomson, S., Hibsch, C., Zingg, A., Holzner, P., Ring, U., Duchêne, S., 2009. Cenozoic tectonic evolution of Naxos Island through a multi-faceted approach of fission-track analysis. Geological Society of London 321, 17.
Thompson, A.B., England, P.C., 1984. Pressure–temperature–time path of regional metamorphism 2: Their inference and interpretation using mineral assemblages in metamorphic rocks. Journal of Petrology 25, 26.
Tirel, C., Brun, J.P., Burov, E., 2004. Thermomechanical modeling of extensional gneiss domes. In: Whitney, D.L., Teyssier, C., Siddoway, C.S. (Eds.), Gneiss Domes in Orogeny. Geological Society of America, Boulder, Colorado, pp. 67–78.
Tirel, C., Brun, J.P., Burov, E., 2008. Dynamics and structural development of metamorphic core complexes. Journal of Geophysical Research, B: Solid Earth 113, 25.
Tirel, C., Gautier, P., Hinsbergen, D.J.J.V., Wortel, M.J.R., 2009. Sequential development of interfering metamorphic core complexes: numerical experiments and comparison with the Cyclades, Greece. The Geological Society, London, Special Publications 311, 257–292.
Trotet, F., Vidal, O., Jolivet, L., 2001. Exhumation of Syros and Sifnos metamorphic rocks (Cyclades, Greece). New constraints on the P–T paths. European Journal of Mineralogy 13, 901–920.
Turcotte, D.L., Schubert, G., 2002. Geodynamics. Cambridge University Press, Cambridge.
Van Den Driessche, J., Brun, J.P., 1992. Tectonic evolution of the Montagne Noire (French Massif-Central): a model of extensional gneiss dome. Geodinamica Acta 5, 85–99.
Vanderhaeghe, O., 2004. Structural development of the Naxos migmatite dome. The Geological Society of America Special Paper 380, 18.
Vanderhaeghe, O., 2009. Migmatites, granites and orogeny: flow modes of partially-molten rocks and magmas associated with melt/solid segregation in orogenic belts. Tectonophysics 477, 119–134.
Vanderhaeghe, O., Medvedev, S., Fullsack, P., Beaumont, C., Jamieson, R.A., 2003. Evolution of orogenic wedges and Continental Plateaux: insights from crustal thermal-mechanical models overlying Subducting Mantle Lithosphere. Geophysical Journal International 153, 27–51.
Vandermolen, I., Paterson, M.S., 1979. Experimental deformation of partially-melted granite. Contributions to Mineralogy and Petrology 70, 299–318.
Vigneresse, J.L., Barbey, P., Cuney, M., 1996. Rheological transitions during partial melting and crystallization with application to felsic magma segregation and transfer. Journal of Petrology 37, 21.
Von Blanckenburg, F., Davies, J.H., 1995. Slab breakoff: a model for syncollisional magmatism and tectonics in the Alps. Tectonics 14, 120–131.
vonQuadt, A., Peytcheva, I., 2005. The Southern Extension of the Srednogorie Type Upper Cretaceous Magmatism in Rila-Western Rhodopes: constraints from isotope geochronological and geochemical data. bulgarian Geological Society 80th anniversary, 3.
Whitney, D.L., Teyssier, C., Siddoway, C.S., 2004a. Gneiss domes in orogeny. The Geological Society of America.
Whitney, D.L., Teyssier, C., Vanderhaeghe, O., 2004b. Gneiss domes and crustal flow. In: Whitney, D.L., Teyssier, C., Siddoway, C.S. (Eds.), Gneiss Domes in Orogeny. Geological Society of America, Boulder, Colorado, pp. 15–33.
Whittington, A.G., Hofmeister, A.M., Nabelek, P.I., 2009. Temperature-dependent thermal diffusivity of the Earth's crust and implications for magmatism. Nature 458, 319–321.
Wijbrans, J.R., McDougall, I., 1986. ^{40}ar/^{39}ar dating of white micas from an Alpine high-pressure metamorphic belt on Naxos (Greece): the resetting of the argon isotopic system. Contributions to Mineralogy and Petrology 93, 7.